To the Graduate Council:

I am submitting herewith a thesis written by Anthony J. Caldanaro Jr. entitled "Trading Space for Time: An Example of Fold Development from the Central Appalachians." I have examined the final copy of this thesis for form and content and recommend that it be accepted in partial fulfillment of the requirements for the degree of Master of Science, with a major in Geology.

Dr. William M. Dunne, Major Professor

We have read this thesis and
recommend its acceptance:

Accepted for the Council:

Associate Vice Chancellor and
the Dean of The Graduate School

STATEMENT OF PERMISSION TO USE

In presenting this thesis in partial fulfillment of the requirements for a Master's degree at the University of Tennessee, Knoxville, I agree that the Library shall make it available to borrowers under the rules of the Library. Brief quotations from this thesis are allowable without special permission, provided that accurate acknowledgment of the source is made.

Permission for extensive quotation from or reproduction of this thesis may be granted by my major professor, or in his absence, by the Head of Interlibrary Services when, in the opinion of either, the proposed use of the material is for scholarly purposes. Any copying or use of the material in this thesis for financial gain shall not be allowed without my written permission.

Signature Anthony D Caldarone

Date 1/7/99

TRADING SPACE FOR TIME: AN EXAMPLE OF FOLD DEVELOPMENT FROM THE CENTRAL APPALACHIANS

A Thesis

Presented for the

Master of Science

Degree

The University of Tennessee, Knoxville

Anthony J. Caldanaro Jr.

May, 1994

DEDICATION

This thesis is dedicated to my parents

Anthony John Caldanaro Sr. and Sharon Marie Caldanaro

and to their parents

Anthony (Papa Shawn) and Rose Caldanaro and Derald and Bernice Thompson

for their love, patience and unending support.

ACKNOWLEDGEMENTS

I am very grateful to my advisor, Dr. William M. Dunne for his all his help, advice, encouragement and patience. Bill is especially thanked for teaching me the importance of strain and microstructures in the deformational history of a structure.

I owe a lot to my two committee members, Dr. Robert D. Hatcher Jr. and Dr. Richard T. Williams for valuable discussions and their quick and professional handling of my thesis. I would like to thank Bob specifically for use of his Macintosh computers, the Izusu for a trip to my field area and for his company while we were doing "field work" at various local golf courses. I thank Rick for helping me keep my perspective ("the Earth is a filter"), the office space in his lab my first year here, the unlimited use of the laser printer and for all his assistance with the HP. A big THANK YOU goes to Dr. Charles M. Onasch for being both my mentor and friend, for access to the facilities at BGSU, and for setting me on this path. Thanks Charlie! Dr. RaNaye B. Dreier also deserves a big THANK YOU for her friendship and unending patience. I am very grateful to RaNaye for the internship at ORNL and for the experience I gained working with her on various hydrogeologic problems. Grants awarded to Caldanaro from the Geological Society of America, the American Association of Petroleum Geologists and Sigma Xi supported this thesis work. Funds were also provided by NSF grants EAR-8915949 and EAR-9206617 to Dunne.

Mike Green is thanked for all his help with sampling and field work —remember "if it is not Keefer, it's butter." I would also like to thank Greg Yanagihara for "hanging" out in my field area. A special thanks goes to Brent Couzens for the numerous trips to my field area, especially the one "unexpected" visit (glad I was not driving) and for being a partner in crime, an excellent advisor and one of my best friends. Thanks Dr. Couzens!

I would like to acknowledge the support of all my friends, faculty and colleagues here at the University of Tennessee. I would especially like to thank the members of the "Old Guard:" Marvin Bennett, Jeff and Kelly Connelly, Marta and Joe Corbin, Tim and

Sally Davis, Landon Davidson, Joachim Dorsch, Kelly Gardener and Chris Olson, Mike Green and Barb Pinto, Amy Halleran and Brian Sheldon, Ralph Harvey, Jim Heller, Maria Leary and Ian Richards, Beth McClellan, Michael Neton, Kathy and Kevin (and Gregory!) Smart, Tony Tingle (the "other" Tony), Ken ("Q") Tobin, Kent Waggoner (and Sylvia), Karen Walker, Greg Yanagihara and anyone else I forgot to name, for making my years here at UT very enjoyable.

In particular I'd like to thank Marta Corbin for being a great friend, for always listening and for graciously losing whenever we played tennis; Maria Leary for just being herself; Ellen Williams for the trips to the lake house, the hiking, and all the tennis and golf; Ian Richards for being from "Down-Under" and for being a good "mate"; Mike Green for his sense of humor and unparalleled enthusiasm for science; Chris Olson for the fireworks display every Labor day, and for being the TFP (total football package); Jim Heller for being the Buddha; Greg Yanagihara for sticking it out with me for 3.5 years; Karen Thorbjornsen and Kevin Smart for being great office-mates. A special thanks goes to Kevin for living up to his name sake. I would also acknowledge all the secretaries Melody, Cindy, Denise, Jayne, Nancy and Gina for all the friendly smiles, assistance, and for putting up with me. Additionally I thank the musicians of the Rock group Rush for their music, the inspiration and "the words that touch my heart."

I wish to thank my parents, Tony and Sharon, my brother Jon and sister Gina for all their support, both financially and morally and for being patient and understanding for all these years. Last but not least, I owe special thanks to Bosiljka Glumac for all her support, encouragement, and concern. I would also like to thank her for feeding and taking care of me and most importantly I thank Bosiljka for being my very best friend!

This thesis has been brought to you by the letter S and the letter T!

ABSTRACT

Many investigators have postulated that deformation near a fold termination is equivalent to deformation during early amplification at the fold culmination. This concept is informally known as "trading space for time" when analyzing the deformation history of any structure. A purpose of this study is to test this concept, using a three-dimensionally exposed, periclinal thrust-modified buckle fold. The target anticline, located in eastern West Virginia, is a second-order parasite in the southeastern limb of a map-scale anticline, is 300 m long, deforms a 9 m thick quartz arenite of the Keefer Sandstone, and was examined primarily across three axial-perpendicular profiles from termination to culmination. These profiles in different parts of the fold share some similarities that might be consistent with the concept of "trading space for time:" NW-verging asymmetry, curved hinges with straight limbs, bedding-parallel slip as a common folding mechanism, and a late-stage set of vertical cross-axial veins. Many specific structural features at the termination are however, absent in the culmination: (1) ubiquitous bed-normal, strike-parallel veins accommodating outer-arc extension; (2) intensification of the layer-parallel shortening (LPS) strain by bed-normal transgranular stylolites and bed-parallel fluid inclusion planes (FIPS); and (3) a lack of outer-arc shortening structures to accommodate the decrease in curvature if the culmination had evolved sequentially from an equivalent of the fold shape to the termination. Similarly, the fold culmination for a thrust-related second anticlinal hinge lacks evidence for these features. Consequently, the fold culmination did not evolve from the termination and "space may not be traded for time."

The deformation history of the quartz arenite ranged from diagenetic compaction through folding where temperatures were 165°-285°C and lithostatic pressures were 150-225 MPa. Deformation progressed from pervasive grain-to-grain solution during compaction to grain-to-grain solution with localized development of transgranular stylolites and FIPS during LPS. Subsequent deformation during folding became even

more heterogeneously distributed with micro- and mesoscale veins, and late-stage intense solution along preexisting faults and bedding surfaces. This increased scale of deformation dominated by mesoscale solution and fracture may have resulted from a loss of porosity for fluid conduits, and a lack of sufficient temperature and/or differential stress to generate dislocation-related intragranular structures.

TABLE OF CONTENTS

SECTION PAGE

1. Introduction 1

2. Geologic Setting 5

3. Fold Geometries and Mesostructures 17

4. Microstructures 21

5. Finite Strain Analysis 30

6. Grain-to-Grain Solution 36

7. Fold Development 46

8. Conclusions 50

REFERENCES 51

APPENDIXES 56

APPENDIX A. ORIENTATION DATA, SAMPLE PREPARATION AND DATA COLLECTION 57

Sample and station orientation data 58

Sample Preparation 62

Data Collection 64

APPENDIX B. TWO- AND THREE-DIMENSIONAL ROTATED AND UNROTATED FINITE STRAIN DATA 66

APPENDIX C. TWO- AND THREE-DIMENSIONAL ROTATED PSS INCREMENTAL STRAIN DATA 77

VITA 81

LIST OF TABLES

TABLE PAGE

1. Microstructure abundances, geometries and strain magnitudes 22
2. Percentages of intragranular microstructures 26
3. Strain ellipses measured with PSS method 37
4. Percentage of silica cement in quartz arenite samples 38

A.1. Bedding orientations of samples 60

B.1. Sample labeling key 66

B.2. Two- and three-dimensional rotated finite strain data 67

B.3. Two- and three-dimensional unrotated finite strain data 72

C.1. Two- and three-dimensional rotated incremental PSS strain data 79

LIST OF FIGURES

FIGURE PAGE

1. Conceptual model of an ideal self-similar thrust sheet 2
2. Stratigraphic column and geologic map in Baker Quadrangle, Hardy County, West Virginia 6
3. Map showing the exposures of the Keefer Sandstone in first- and second-order parasitic folds to the Hanging Rock anticline 8
4. (a) Cross section along line A-A' of Fig. 3 10
5. Dominant mesostructures and microstructural suites in study area 13
6. (a) O-O' outcrop with view to NE along the fold axis and hammer for scale 15
7. Representative microstructures 23
8. Equal-area lower hemisphere stereonets depicting finite strain ellipsoid axial orientations in the host syncline, and profiles O-O', M-M' and I-I' 31
9. Flinn plots of finite strain data in the host syncline, and profiles O-O', M-M' and I-I' 33
10. Equal-area lower hemisphere stereonets depicting PSS incremental strain ellipsoid axial orientations for the host syncline, and profiles O-O', M-M' and I-I' 40

A.1. Keefer Sandstone exposure map showing sample and station locations 59

A.2. Block of Keefer Sandstone 62

A.3. Orientaion of billets on glass slides 63

A.4. Sample labeling convention 63

A.5. Set-up for CL photomicroscopy 64

A.6. Orientation of photographs on the digitizing pad 64

1. INTRODUCTION

An intriguing question in structural geology is whether the state of deformation at one position along a structure is equivalent to the state of deformation in the past or future at another position within the same structure. In essence, can space be traded for time, when examining the three-dimensional deformation history of a structure, such as a fold? Kinematic models (Suppe 1983, Suppe & Medwedeff 1990) for thrust-related folds have been proposed that yield a geometry where space may be traded for time from culmination to termination (Fig. 1). Also, comparison of analog model results to natural three-dimensional geometries for buckle folds has been used to indicate that space may be traded for time in the study of their three-dimensional deformation histories (Dubey & Cobbold 1977). If these relationships are correct, a powerful approach in fold analysis is created: The analysis of the deformation history at a fold culmination completely describes the deformation history for other profiles across the fold because earlier states of deformation at the culmination are equivalent to final states of deformation at some distance along the fold axis. Hereafter, we will describe this approach as the behavior of "trading space for time."

Only one of three studies (Nickelsen 1979, Bamford & Ford 1990, Fischer & Woodward 1990) about three-dimensional fold development has directly addressed this possible relationship. Using well-constrained subsurface geometries, Fischer & Woodward (1990) found that the growth of a map-scale thrust-related anticline changed in three dimensions as a function of local intrinsic properties (e.g., pore fluid pressure, stratigraphy, structural position) that varied in both space and time during deformation. Space could not be traded for time in this three-dimensional deformation history. Also, Dubey & Cobbold (1977) showed that this type of behavior ceased when folds interfered in three dimensions as a result of hinge propagation. Yet, the ubiquity and consistent temporal relations of the structures that resulted from the elegant deformation sequence for the "whaleback" anticline at the Bear Valley Strip Mine (Nickelsen 1979) may indicate

Fig. 1. Conceptual model of an ideal self-similar thrust sheet (from Fischer & Woodward 1990).

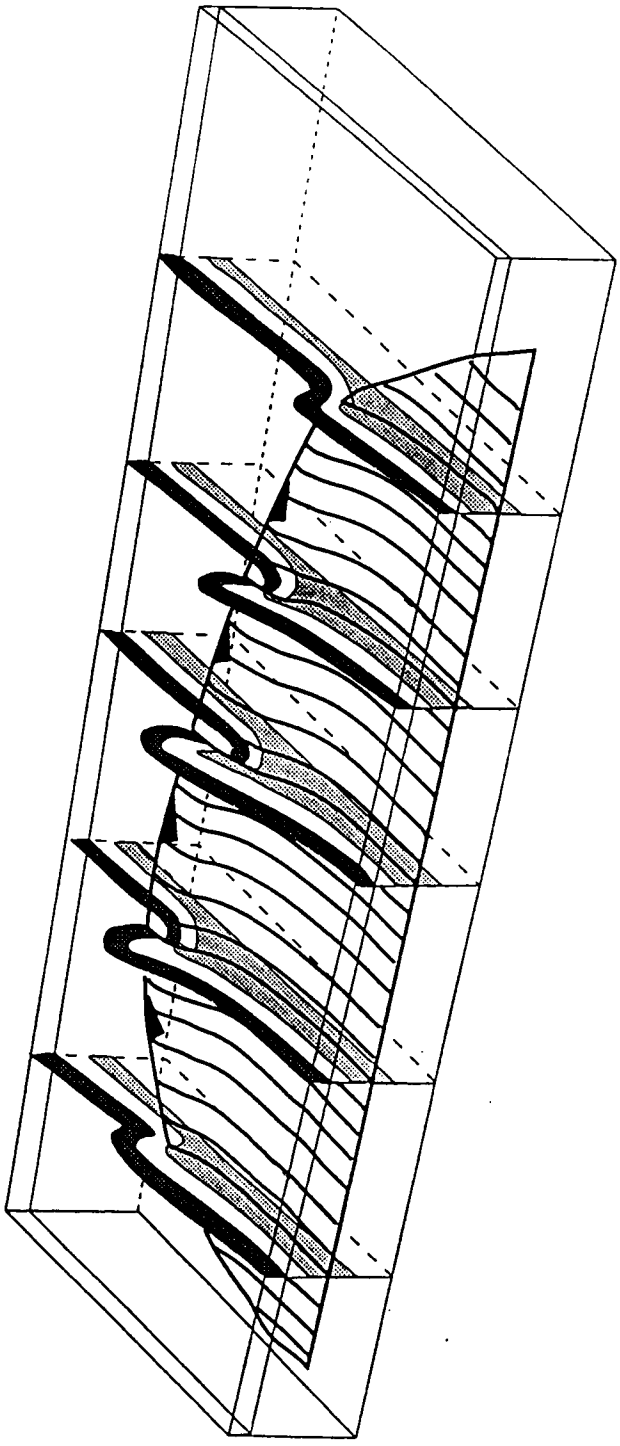

that this behavior was operative in that structure.

One purpose of this study is to test a periclinal fault-related buckle fold to determine if space may be traded for time when examing the deformation history. This study would be the first test of this behavior to include strain and microstructural data, as well as geometric data. As the target monolayer fold consists of quartz arenite, a second purpose of this study is to discuss the deformation behavior of this lithology in conditions of relatively low pressure and low temperature in an orogenic foreland.

2. GEOLOGIC SETTING

The field area is located in the eastern panhandle of West Virginia (Fig. 2) in the Valley and Ridge province of the central Appalachians. The target fold (Fig. 3) is a 300 m long, periclinal, second-order parasitic anticline in the core of a first-order parasitic syncline (hereafter called the host syncline) in the southeastern limb of the Hanging Rock anticline (Fig. 2) (Ferrill & Dunne 1989). The Hanging Rock anticline is part of the Cacapon Mountain anticlinorium (Fig. 2), which deforms a roof sequence over an Alleghanian blind duplex containing thrusted Cambro-Ordovician carbonates (Gwinn 1964, Rodgers 1970, Perry 1978, Kulander & Dean 1986, Ferrill & Dunne 1989).

The second-order parasitic anticline deformed a thick-bedded quartz arenite of 9 m thickness, which comprises the Silurian Keefer Sandstone. This anticline offers several advantages to this type of study: (1) A resistant, nearly monomineralic rock type that is well exposed in three dimensions. The fold is exposed along its axis in three profiles (O-O', M-M' and I-I') with additional intermittent exposures between profiles and continuous exposures in the limbs of the host syncline (Fig. 3). (2) Up to 9 m of unit thickness offers greater sampling sensitivity across fold profiles than in previous field-based studies of thinner-bedded folds (e.g., Groshong 1975, Narahara & Wiltschko 1986). (3) The grain supported fabric (Folk 1960) is well suited to spatial strain measurement techniques (Fry 1979), such as the normalized Fry method (Erslev 1988) (Appendix A, B). (4) The Keefer Sandstone is effectively an isolated monolayer interbedded with an underlying 122 m of soft, shale-dominated Rose Hill Formation and overlying 81 m of soft, thin, interbedded calcareous shale and limestones of the McKenzie Formation (Figs. 2, 4) (Tilton et al. 1927). The monolayer behavior eliminates the effects of intraphase fold interference from multilayer folding (Ramberg 1964) that could complicate the analysis of the deformation history. (5) The fold lacks a deformation history complicated by intraphase interference from hinge propagation (Dubey & Cobbold 1977) because other folds are not present

Fig. 2. Stratigraphic column and geologic map in Baker Quadrangle, Hardy County, West Virginia (from Ferrill & Dunne 1989). Black rectangle shows location of field area (Fig. 3) with respect to the Hanging Rock and Baker Mountain anticlines (HRA & BMA). Inset regional map of West Virginia shows location of main map and position of the Cacapon Mountain anticlinorium (CMA).

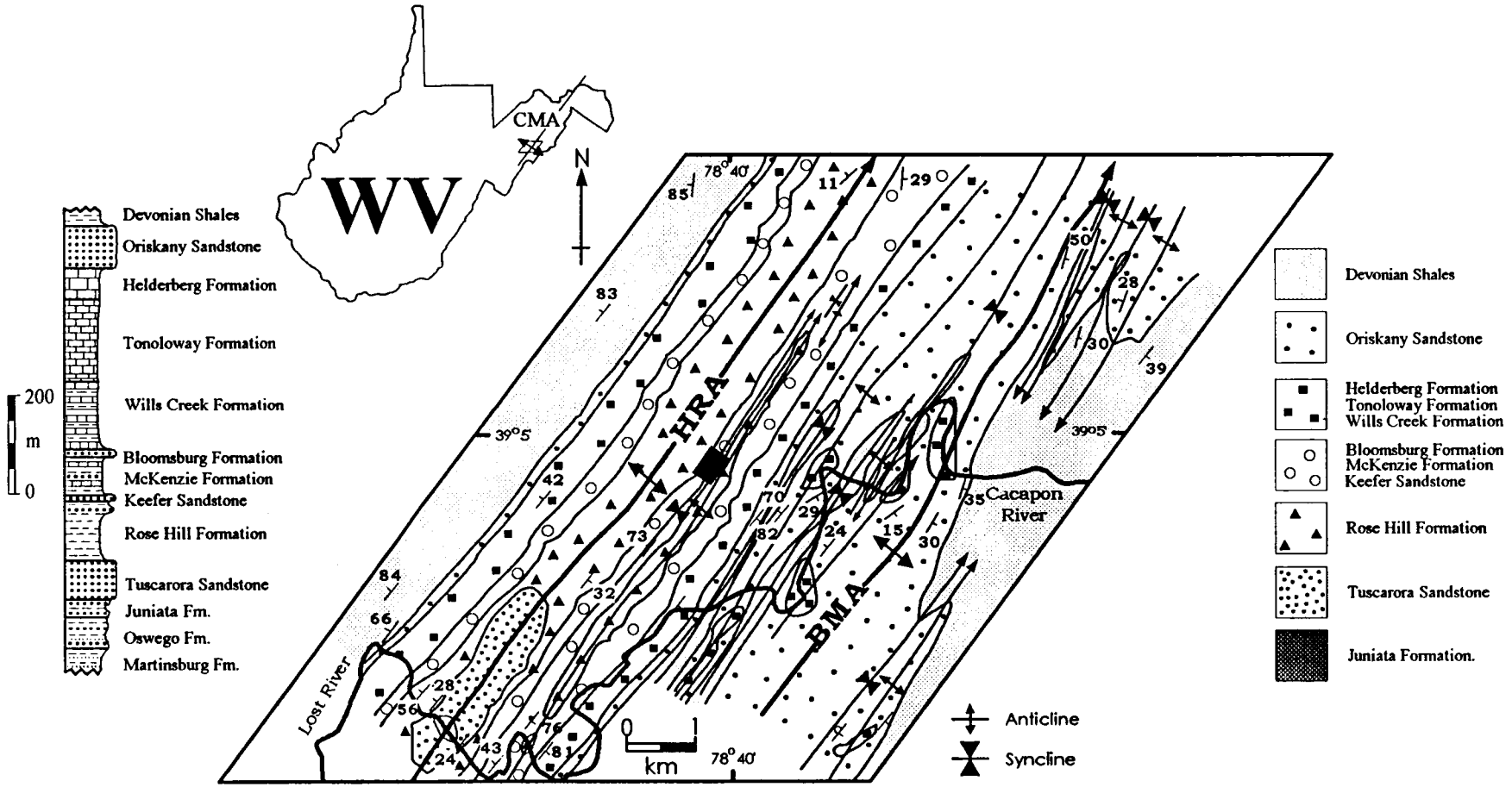
WV
CMA
N
Devonian Shales
Oriskany Sandstone
Helderberg Formation
Tonoloway Formation
Wills Creek Formation
Bloomsburg Formation
McKenzie Formation
Keefer Sandstone
Rose Hill Formation
Tuscarora Sandstone
Juniata Fm.
Oswego Fm.
Martinsburg Fm.
200
m
0
78°40'
39°5'
HRA
BMA
Cacapon River
Lost River
km
Anticline
Syncline
Devonian Shales
Oriskany Sandstone
Helderberg Formation
Tonoloway Formation
Wills Creek Formation
Bloomsburg Formation
McKenzie Formation
Keefer Sandstone
Rose Hill Formation
Tuscarora Sandstone
Juniata Formation.

Fig. 3. Map showing the exposures of the Keefer Sandstone in first- and second-order parasitic folds to the Hanging Rock anticline. The locations of profiles O-O', M-M' and I-I' in the target anticline of Fig. 5, and cross section lines A-A' and B-B' of Fig. 4 are shown.

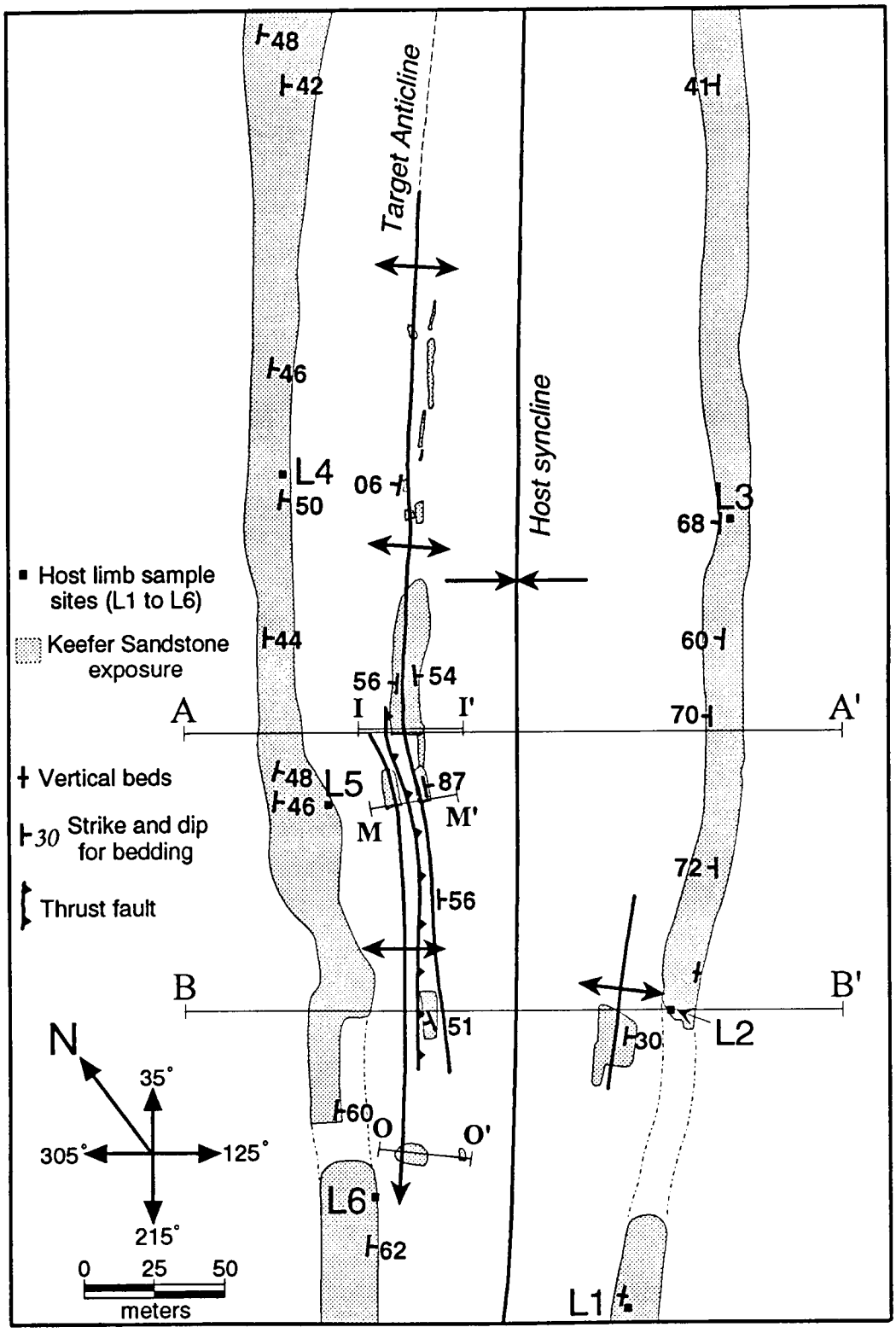
Target Anticline
Host syncline
48
42
41
46
L4
50
06
L3
68
Host limb sample sites (L1 to L6)
Keefer Sandstone exposure
44
60
56
54
A
I
I'
70
A'
Vertical beds
48
L5
87
46
M
M'
30 Strike and dip for bedding
72
Thrust fault
56
B
B'
51
30
L2
N
35°
305°
125°
215°
60
O
O'
L6
62
L1
0
25
50
meters

Fig. 4. (a) Cross section along line A-A' of Fig. 3. (b) Cross section along line B-B' of Fig. 3.

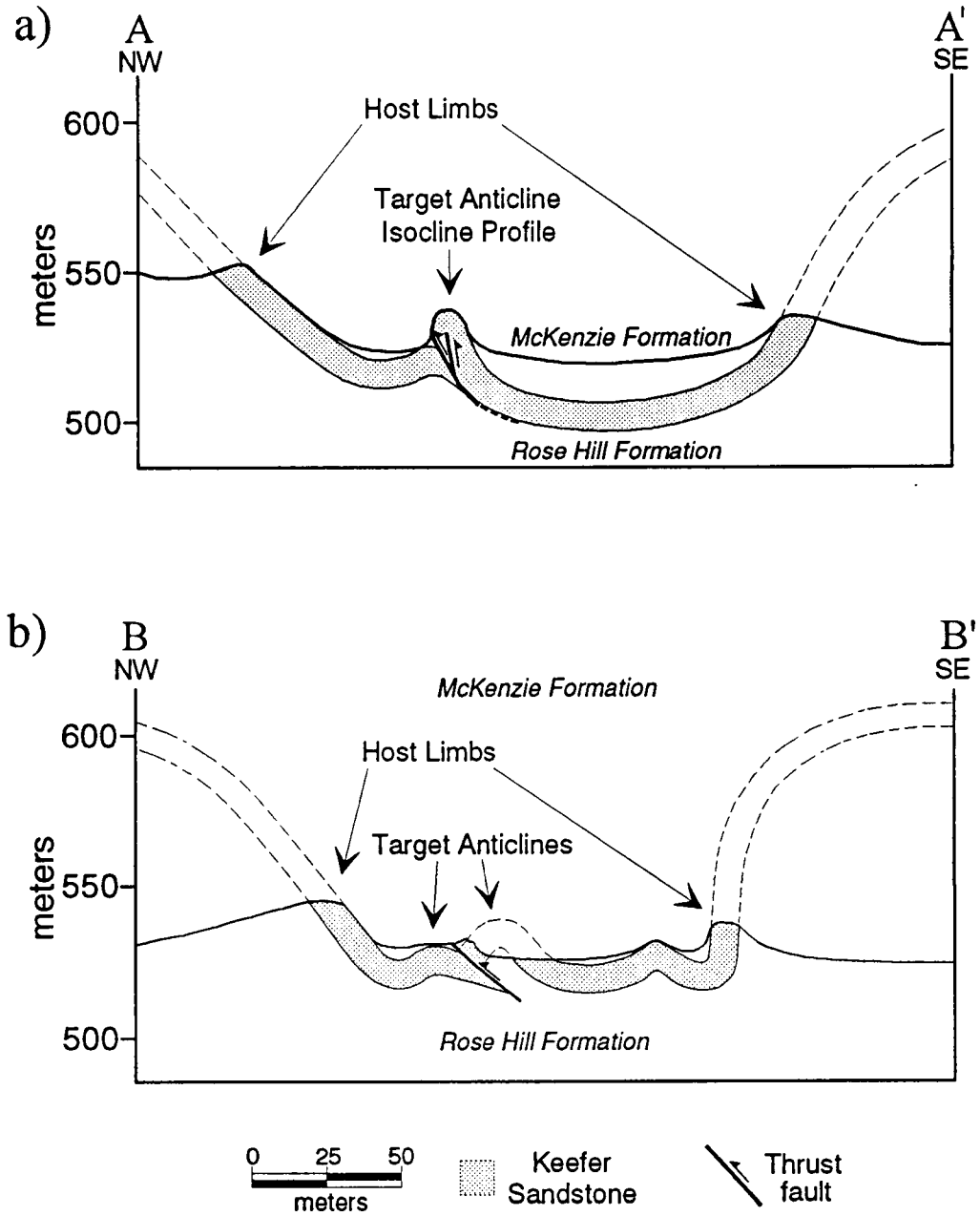
a)
A
NW
A'
SE
600
550
500
meters
Host Limbs
Target Anticline
Isocline Profile
McKenzie Formation
Rose Hill Formation
b)
B
NW
B'
SE
McKenzie Formation
600
550
500
meters
Host Limbs
Target Anticlines
Rose Hill Formation
0
25
50
meters
Keefer
Sandstone
Thrust
fault

along strike (Fig. 3).

The concept of "trading space for time" involves several implicit assumptions and they were applied to the target anticline: (1) The most deformed part of a fold, i.e. the part with the greatest amplitude, is the oldest; and (2) Folding began at the present location of the anticlinal and propagated along the hinge line. Applying these assumptions, the approach in this study was to examine three strike-normal profiles (O-O', M-M' and I-I', Fig. 3) across a three-dimensionally exposed fold from termination to culmination (Figs. 2, 3). The profiles were constructed from field observations and photographs taken along the fold hinge (Figs. 5, 6) to show sample locations, fold profile geometries, and the distribution of various structural data sets. Data sets collected at each profile include: bedding and fold-axis orientations (Appendix A), fold interlimb angles, fold vergence, and both meso- and microstructure abundances and geometries. Incremental and finite strain data were also collected along the fold, but were not plotted on the profiles.

Fig. 5. Dominant mesostructures and microstructural suites in study area. (a) Host syncline limbs. (b) O-O' profile. (c) M-M' profile. (d) I-I' profile. Symbols represent: black square-microstructural Suite I, white square-microstructural Suite II, black triangle-microstructural Suite III, white triangle-microstructural Suite IV, black circle-microstructural Suite V, white circle-microstructural Suite VI, black star-microstructural Suite VII, white star-microstructural Suite VIII, black diamond-microstructural Suite IX, white diamond-microstructural Suite X (see text for explanation).

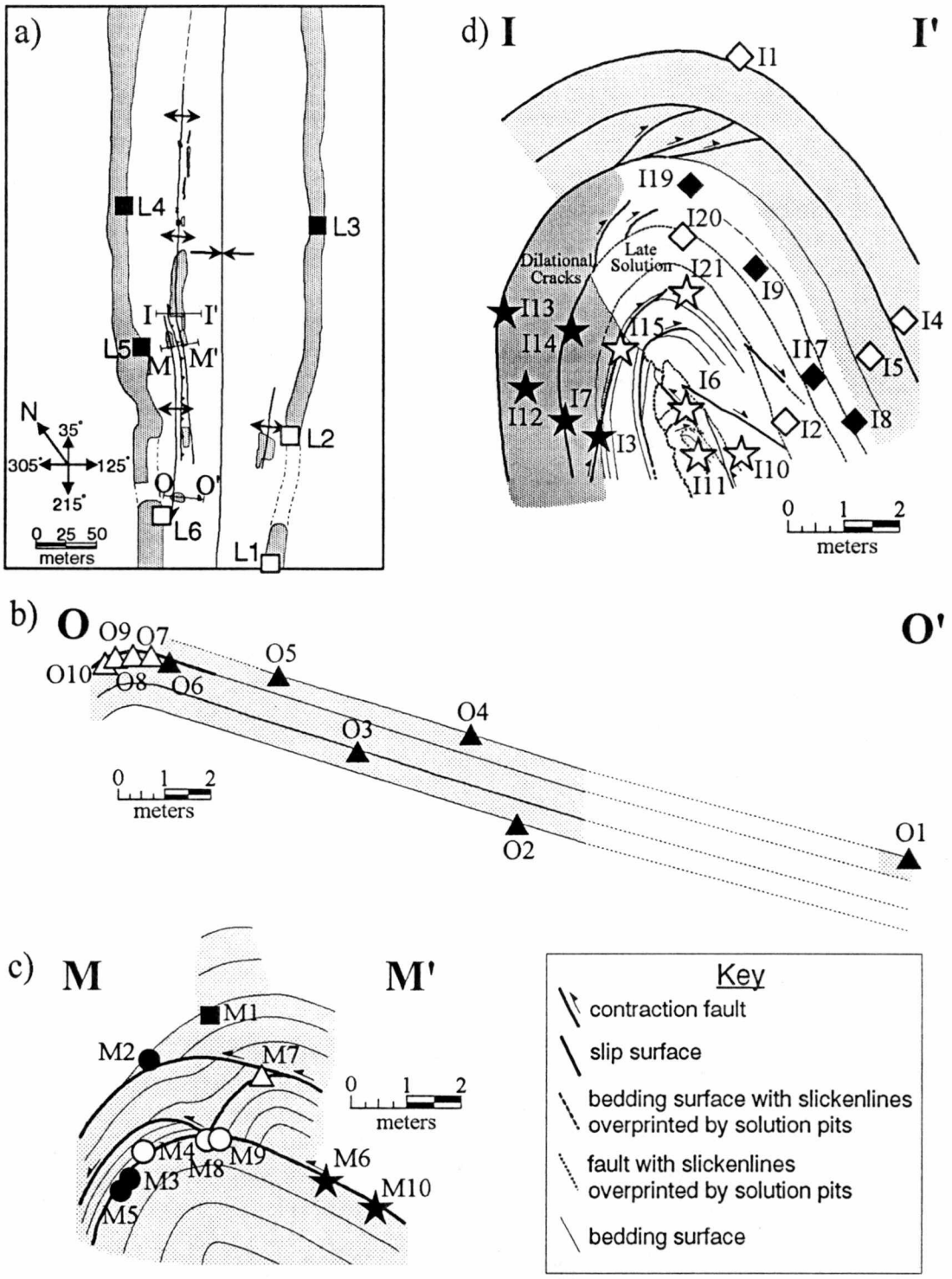
a)
L4
L3
I
I'
L5
M
M'
N
35°
305°
125°
215°
O
O'
L6
L2
L1
0 25 50
meters
d) I
I'
I1
I19
I20
Dilational Cracks
Late Solution
I21
I9
I13
I14
I15
I4
I17
I5
I6
I7
I12
I3
I2
I8
I11
I10
0 1 2
meters
b) O
O9
O7
O10
O8
O6
O5
O4
O3
O2
O1
O'
0 1 2
meters
c) M
M'
M1
M2
M7
0 1 2
meters
M4
M9
M6
M8
M3
M10
M5
Key
contraction fault
slip surface
bedding surface with slickenlines overprinted by solution pits
fault with slickenlines overprinted by solution pits
bedding surface

Fig. 6. (a) O-O' outcrop with view to NE along the fold axis and hammer for scale. (b) M-M' outcrop with view to the NE along the fold axis and hammer for scale. (c) I-I' outcrop with view to the NE, profile is 8.8 m in height. (d) fold core at I-I' showing prominent late-stage solution on faults and bedding. Top to the left. (e) Solution pitting of slickenlines (horizontal in photograph) in Domain 1 at I-I' on bottom of layer 5 in Fig. 5. Top to the left. (f) Bed-oblique to normal veins in Domain 2 in layers 4 and 5 (Fig. 5.) of the NW limb of I-I'.

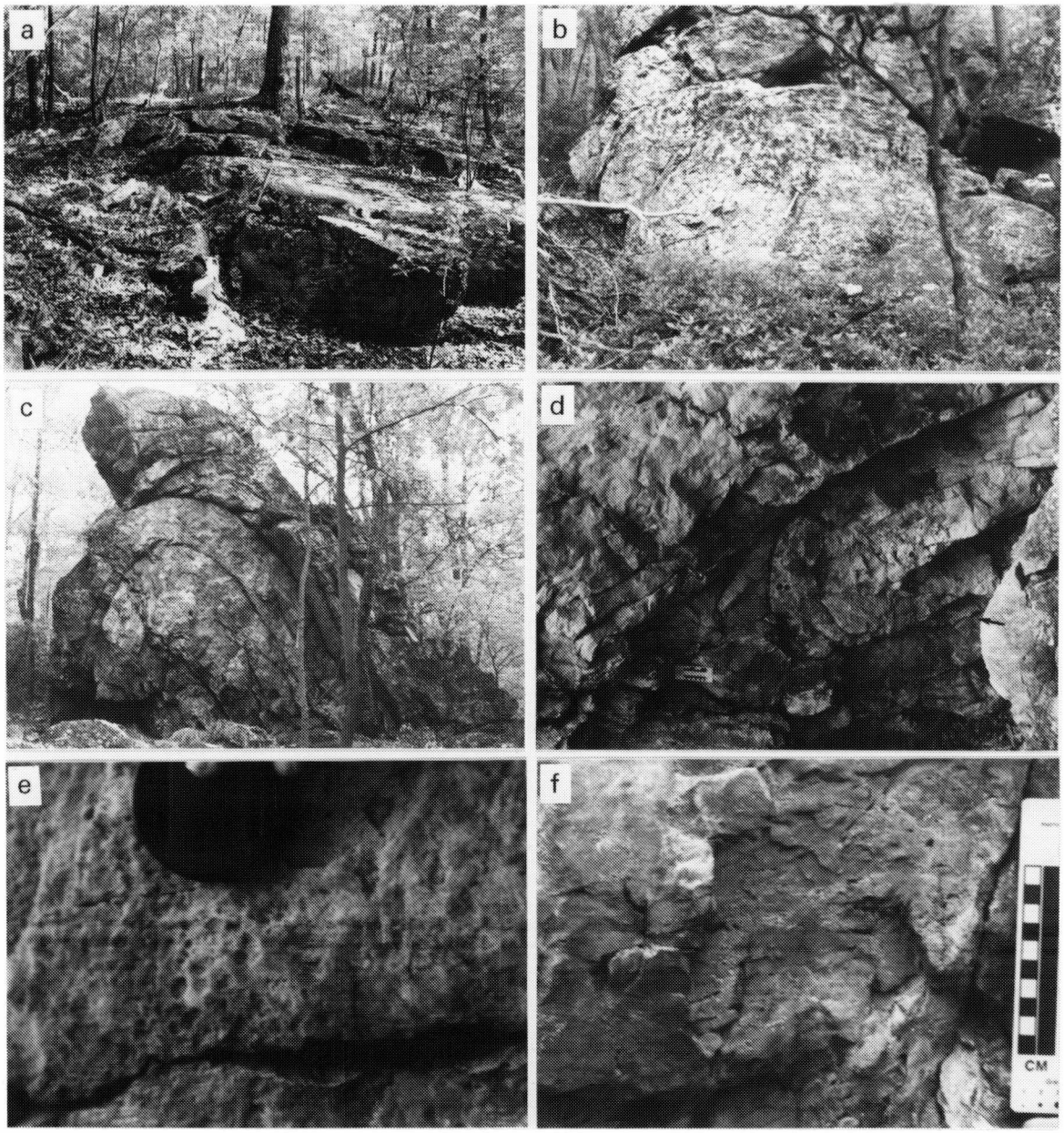
a
b
c
d
e
f
CM

3. FOLD GEOMETRIES AND MESOSTRUCTURES

Host syncline

The host syncline (Figs. 3, 4, 5a) verges northwest with a more steeply dipping southeastern limb, and has an axial orientation of 222/02. Both limbs decrease in bed dip to the northeast as the fold widens and parasitic folds disappear. Cross sections for the syncline (Fig. 4) were constructed, assuming: (1) preservation of bed-normal thickness in the Keefer Sandstone; (2) surficial fault geometry and position restricts subsurface thrust geometry; (3) measured surface dips project into the subsurface; and (4) a minimum subsurface amplitude for the host syncline.

The syncline limbs contain bedding-parallel, dip-parallel slickenlines, providing evidence of layer-parallel slip. The slip surfaces are ornamented with abundant polished groove slickenlines that have less than 1 mm of relief and 5 mm of width. These slip-ornamented bedding surfaces define mechanical layer thicknesses of 0.5 to 2 m in the southeast limb with 7 slip surfaces and 1 to 3 m in the northwest limb with 3 slip surfaces. The northwestern limb contains a few minor contraction faults (less than 0.5 m displacement), but is otherwise not extensively fractured. Where the southeastern limb is steeper (samples L1, L2 in Fig. 3), abundant fractures are developed. The oldest mesofractures are numerous strike-normal, white "hairline" veins. These fractures are cut by larger, more abundant subparallel-to-strike fractures with a weathered brown fill. The sequence of vein formation may be interpreted to represent strike-parallel, layer-parallel extension followed by dip-parallel, layer-parallel extension.

O-O' profile

The termination of the parasitic anticline has one narrow rounded hinge, two straight limbs, and an open geometry with a 113° interlimb angle (O-O' in Figs. 3, 5b, 6a). The fold axis orientation is 216/03. Dip-parallel slickenlines on bedding cross the fold

hinge, indicating that the hinge was not always a pinpoint during folding (Stewart & Alvarez 1991). Also, the profile contains 110° to 120° trending, vertical white "hairline" veins with a 10 to 40 cm spacing.

M-M' profile

The anticlinal hinge broadens but tightens to an interlimb angle of 79° from O-O' to M-M' (Fig. 3). Across M-M' the fold hinge doubly plunges 204/02 at the southwest end and 010/02 at the northeast end, indicating the presence of a culmination along the hinge line. Mesostructurally, the M-M' profile is dominated by bedding-slip surfaces and contraction faults (Figs. 5c, 6b). The faults and bedding slip surfaces are ornamented with smooth, polished slickenlines which are again less than 1 mm high and 5 mm wide. The slickenlines are oriented normal to strike, indicating dip-parallel displacement. Three contraction faults branch from the bedding-slip surfaces with NW displacements of 0.5 to greater than 5 m (Fig. 5c). They transported Keefer Sandstone of the southeastern limb through the hinge and into the NW limb, again indicating that the anticlinal hinge was not a pinpoint through folding. They occur in the footwall of the thrust that emplaces the second anticlinal hinge of the fold, which is visible in the I-I' profile (Figs. 3, 4, 5c & d). Also, vertical white "hairline" veins, trending 110 to 113° as in the O-O' profile are developed within M-M'.

I-I' profile

This profile (Fig. 5d) contains the fold culmination for the second anticlinal hinge (I-I', Fig. 3) that is displaced about 7 m onto the main hinge along a thrust (Fig. 4). The angle of the thrust fault to bedding between M-M' and I-I' is 34°, as determined by assuming that the angle of the thrust through the footwall ramp is parallel to the bedding dip in the hanging wall, where the angle of the fault to bedding is the difference between the bedding dips of the footwall and hanging wall (Fig. 4a). The exact mode of formation

for this thrust fault, as either a fault-propagation, fault-bend or some other kinematic variant, could not be determined from the available field data and so the term "thrust-related fold" is applied to this anticlinal hinge. It will be shown that this lack of knowledge is not crucial for addressing the problem at hand.

The thrust-related anticlinal hinge is isoclinal (Figs. 5d, 6c), the northwest limb is a hanging wall ramp to the thrust, and basal Keefer Sandstone contacts basal Keefer Sandstone with no intervening Rose Hill Formation in the innermost core of the fold (Figs. 5d, 6c & d). This geometry is kinematically interpreted to be the result of liftoff folding (Namson 1981) of the Keefer Sandstone from a detachment in the Upper Rose Hill Formation during formation of the imbricate thrust. The culmination is a long "whaleback" exposure (Fig. 3) where the hinge trends 033/01. The entire fold profile is transected by vertical white "hairline" veins trending 105 to 115° as found in the other two profiles.

The anticline contains eight bedding-slip surfaces at about 0.7 m intervals (Fig. 5d) that are continuous through the fold hinge and ornamented with the typical slickenline morphology. This outcrop of Keefer Sandstone has the greatest number of bed-parallel slip surfaces, which may indicate greater total slip. Also, the continuity of the slip surfaces through the fold hinge, again indicates the lack of a permanent pinpoint during folding.

Two sets of contraction faults are present within the isoclinal hinge. The younger faults offset most other mesostructures, including some bedding-parallel slip surfaces, are located in the hinge and southeastern limb, and displace hanging walls to the southeast. Several faults exploit crossbeds (Fig. 6d) and aid hinge thickening, which totals 1.32 m (Fig. 5d). The older faults are restricted to the inner hinge where they are overprinted by solution pitting (Fig. 5d).

Two distinct mesostructural domains are discernible in the I-I' profile, Domain 1 and 2. Domain 1 occupies the inner layers of the hinge and southeastern limb (clear field,

Fig. 5d) and is characterized by reactivation of bedding slip surfaces and contraction faults as solution surfaces. The occurrence of solution features increases from the southeastern limb towards the core as the solution morphology changes from isolated pitting (Fig. 6e) to a weakly-preserved slip lineation with pronounced pitting. In the fold core, all evidence of displacement is destroyed by solution except for the bed offsets and older contraction faults which have up to 8 cm of relief from tectonic solution. Kinematically, the domain is characterized by a subhorizontal shortening that intensifies from the SE limb to hinge.

Domain 2 in the adjacent NW limb (dark gray field, Fig. 5d) lacks this shortening deformation, but is characterized by strike-parallel, bed-normal veins that transect older bedding-slip surfaces. These veins occur as both isolated fractures and as arrays of en-echelon fractures (Fig. 6f). The veins are interpreted to have accommodated dip- and bedding-parallel extension after bedding slip.

4. MICROSTRUCTURES

Forty-nine oriented samples were collected to identify microstructural suites (Fig. 5, Table 1) and to use for strain analysis. For each sample, three mutually perpendicular thin sections were cut: parallel to bedding (b-section); normal to bedding and parallel to strike (p-section); and normal to bedding and perpendicular to strike (v-section) (Appendix A). The geometries and age relationships of microstructures were noted for each sample in both transmitted light and cathodoluminescence, and used to define ten microstructural suites (Wu et al. 1991, Onasch 1990, Onasch & Dunne 1993). Microstructures in the quartz arenite include: (1) grain-to-grain solution surfaces; (2) transgranular solution surfaces; (3) undulatory extinction; (4) deformation lamellae and deformation bands; (5) fluid inclusion planes (FIPS); (6) microveins; (7) microfaults; and (8) fracture-related apparent intragranular structures (FRAIS) (Fig. 7). Extensional strains for the microveins and FIPS were measured normal to fracture walls (Onasch 1990), and minimum values of volume loss by tectonic stylolites were estimated by measuring the maximum height of stylolite columns (Stockdale 1926, Heald 1955, Tada & Siever 1989).

Host syncline

The host fold limbs contain two microstructural suites (Fig. 5a, Table 1). Samples L3, L4 and L5 (Suite I) contain negligible tectonic microstructures. These samples are located where bedding dip is less than 50°, the syncline has a wider outcrop (Fig. 3) and structural complexities such as parasitic folds are absent. This microstructural suite is interpreted to indicate that the Keefer Sandstone characteristically lacks micro- and mesostructures unless deformation conditions are locally intensified. Samples L1, L2 and L6 (Suite II) are located where bedding is steep to near vertical, the syncline has narrower outcrop (Fig. 3) and parallel mesofractures are abundant. Suite II is characterized by strike-parallel, bed-perpendicular FIPS and microveins that accommodated 1.6 to 4.9%

Table 1. Microstructure abundances, geometries and strain magnitudes.

Fold Geometry	Sample Number	Microveins					Fluid Inclusion Planes					Stylolites	Fault	Microstructural Suite
		Sp; b-ppd.	Dp; b-ppd	Bed-par.	Do; b-ppd	Bed-oblq.	Sp; b-ppd.	Dp; b-ppd	Bed-par.	Do; b-ppd	Bed-oblq.	Sp; b-ppd.		
	L1	3.0	p				0.2		r					II
	L2	1.1					0.5	p	r					II
Host	L3						p		r					I
Syncline	L4						p							I
	L5						p							I
	L6	4.7					0.2							II
	O1					r					r	p		III
	O2					r					0.2	p		III
	O3			r		0.5			0.6		0.1	p		III
	O4					r			0.1		0.1	p		III
O-O'	O5						r		0.2			p		III
Profile	O6		r					r	0.4	r		p	p	III
	O7	6.6	p					0.8	p			p		IV
	O8	3.6							0.5			p		IV
	O9	5.0				3.2		p	0.2		p	p		IV
	O10	4.6	r			r		r	p			p		IV
	M1						p							I
	M2		p			p		p			p			V
	M3					p					p			V
	M4		p						p			r		VI
M-M'	M5		a			a		a			a			V
Profile	M6	a	a				a	a	p					VII
	M7		p		a			p		a		p		IV
	M8		p					p	a					VI
	M9		p				r	p	a					VI
	M10	a	a				a	a						VII
	I1		0.2					p						X
	I2			0.4				0.2						X
	I3	0.4	2.7					0.4				p		VII
	I4		0.9					0.3						X
	I5	r	4.0	0.5			r	0.6	r			p	p	X
	I6	6.6	3.3	5.8	3.3		0.1	r						VIII
	I7		2.6					r						VII
	I8	2.6	5.2				r	0.5		r		p		IX
I-I'	I9	3.6	5.7	2.3				r				p		IX
Profile	I10	2.0	1.7	1.0			0.2	0.4	0.1			p		VIII
	I11	6.3	3.9	9.2			p	0.3	0.2				p	VIII
	I12	5.8	5.0				0.5	0.6	p	r			p	VII
	I13	1.0	0.6		1.1		r	0.1		0.8				VII
	I14	5.4		4.0			p	0.8	1.5				p	VII
	I15	7.3	2.8	0.7	3.7		p	0.7	0.7			p	a	VIII
	I17	1.7	6.9				0.3	0.7				p		IX
	I19	1.6	0.7				r	0.1				p		IX
	I20		0.8		r			0.1	r	r		p		X
	I21	0.5	2.7				arrays	arrays	p				a	VIII

Sp = strike-parallel; Dp = dip-parallel; Do = dip oblique; Bed-par. = bed-parallel; b-ppd = bed-perpendicular; n/a = not applicible
blank = none observed; a = abundant; p = present; r = rare; number = microfracture strain (percent extension normal to walls)

Fig. 7. Representative microstructures. Bedding is horizontal and scale bar equals 0.5 mm for all photomicrographs. (a) Microvein (MV) with associated mortar texture (MT) in cross-polarized light, sample O6v. (b) Same view as in (a) but under cathodoluminescence (CL). Microveins and their mortar texture luminesce darkly. (c) Example of a fracture-related apparent intragranular structure (FRAIS) in cross-polarized light, sample I14v. (d) Same view as in (c) but under CL showing darkly luminescent microvein defining the FRAIS. (e) Reactivation of multiple episodes of fracturing in plane-polarized light, sample I15v. Bed-parallel fluid inclusion planes (FIP) are cut, and later recut a bed-normal microvein (MV). (f) Same view as in (e) but under CL showing cross-cutting sets of darkly luminescent microveins (MV). (g) Strike-parallel, bed-normal stylolites (SY) in O3. (h) Cathodoluminescent image of sample L3b, showing both grain interpenetrations (I) for the PSS method and straight grain boundaries (SGB).

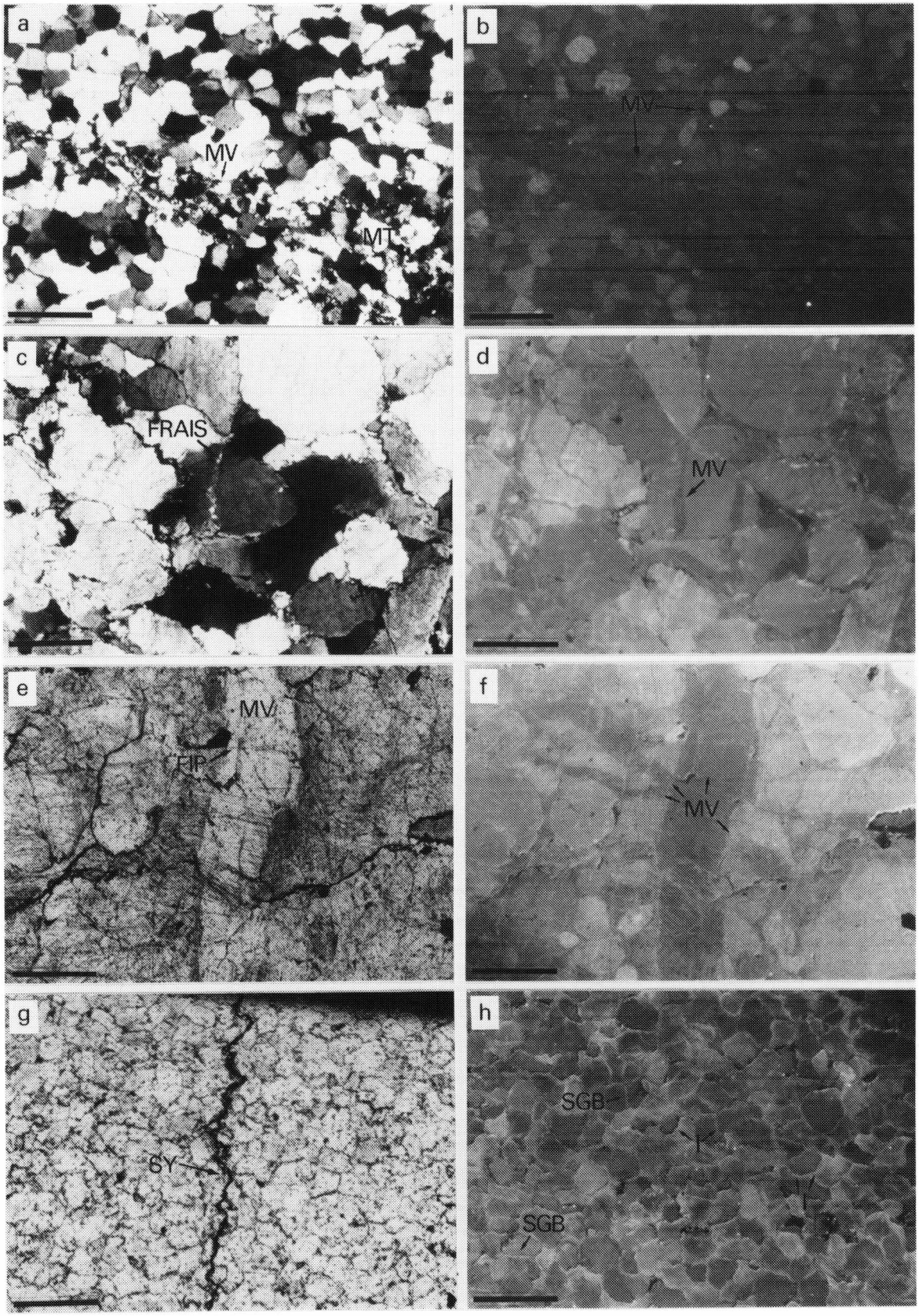
a
MV
MT
b
MV
c
FRAIS
d
MV
e
MV
FIP
f
MV
g
SY
h
SGB
SGB

dip-parallel, bed-perpendicular extension (Fig. 5a, Table 1). In cross-polarized light, the precipitated quartz of the microveins includes linear zones of mortar texture with patchy or subgrain-like extinction in some larger grains (Fig. 7a, Tables 1, 2) (Wu & Groshong 1991, Onasch & Dunne 1993). Mortar texture is an aggregate of fine-grained material that has been interpreted to result from recrystallization around the margins of older deformed grains or possibly as a precursor of cataclasis (Hobbs et al. 1976, Groshong 1988). Using cathodoluminescence (CL) for the Keefer Sandstone samples, the zones of mortar texture are coincident with and indistinguishable from microveins, which dully luminesce unlike the host rock (Fig. 7b). This characteristic is used to infer that the mortar texture represents newly precipitated material in vein fills and not recrystallized grains.

Most subgrain-like extinctions have boundaries decorated by dark lines and small inclusions that are typical of FIPS. The presence of these fracture surfaces is used to infer a discontinuous change in extinction from lattice reorientation by fracturing and not dislocation-related processes. These features are termed fracture related, apparent intragranular structures (FRAIS), and are only developed along the perimeters of microveins (Figs. 7c & d, Table 2).

O-O' profile

O-O' contains two additional microstructural suites (Fig. 5b, Table 1). All samples, contain bed-parallel FIPS (except O1 and O2) with extension magnitudes of 0.1 to 0.6% (Table 1) and strike-parallel, bedding-normal stylolites (Fig. 7g), which are the oldest structures. The stylolites have spacings of 3 to 5 mm, and using column amplitudes (Stockdale 1926), yield an average minimum volume loss of 1.8% in the SE limb and 2.1% in the hinge. The coeval fractures and stylolites accommodated bed-normal extension and layer-parallel shortening throughout the profile, perhaps prior to folding.

Table 2. Percentages of intragranular microstructures.

Sample	N	Nothing	Undulatory Extinction	Subgrains	Deformation lamellae	Deformation bands	FRAIS
L1v	258	48	47	0	0	3	2
L2v	250	50	44	1	0	2	3
L3v	258	45	52	0	0	2	1
O2v	257	47	49	0	0	2	2
O3v	253	44	54	0	0	1	0
O5v	252	52	46	0	0	1	1
O6v	254	49	45	0	0	1	5
O9v	255	55	40	0	0	2	3
M1v	253	57	42	0	0	1	0
M2v	255	42	56	0	0	2	0
M3v	250	65	34	0	0	0	2
I4v	251	61	37	0	0	0	1
I6v	250	51	46	0	0	0	3
I9v	252	41	56	0	0	1	2
I10v	250	59	40	0	0	0	1
I11v	255	53	44	0	0	2	1
I12v	252	65	32	0	0	1	2
I13v	255	64	33	0	2	0	1
I14v	251	64	32	0	0	0	3
I17v	255	60	38	0	0	2	1
I19v	250	68	32	0	0	0	0
I20v	253	64	33	0	0	1	2

N is the number of grains point-counted per sample.

Samples O1 through O6 of Suite III contain only these structures (Fig. 5b), whereas samples O7 to O10 in Suite IV of the anticlinal hinge zone also contain strike-parallel, bedding-normal and bedding-oblique microveins with extensions of 3.6 to 8.2% that overprint the older microstructures. The restriction of these microveins to the hinge zone is interpreted to indicate outer-arc extension by fracture formation.

M-M' profile

In contrast to the host syncline and O-O', M-M' lacks a well-defined distribution of microstructural suites (Fig. 5c, Table 1). For example, the pervasive layer-parallel shortening of O-O' is absent. Five suites are recognized and two suites, Suites V & VI, are unique to this profile. Samples M2, M3 and M5 (Suite V) occur in the northwestern limb and are characterized by bed-perpendicular, dip-parallel and bed-oblique microfractures. Specimens M4, M8 and M9 (Suite VI) in the central hinge area, contain bed-parallel FIPS and bed-normal, dip-parallel microveins with FIPS. Sample M1, like samples L3, L4 and L5 in the host syncline contains negligible microstructures and is placed in Suite I (Fig. 5c). Sample M7, which has bed-perpendicular solution surfaces, bed-parallel FIPS and an overprint of bed-perpendicular and oblique microveins corresponds to samples O7 through O10 (Suite IV). Samples M6 and M10 (Suite VII) from the southeastern limb contain abundant dip-parallel, strike-parallel, and bed-parallel microfractures. The lack of a simple microstructure distribution and the occurrence of unique suites in M-M' may be indicative of localized microfracturing in response to the presence of several contraction faults and their related fault-bend fold hinges (Fig. 5c).

I-I' profile

I-I', unlike M-M', is distinguished by a few simply distributed microstructural suites (Fig. 5d, Table 1). Samples I3, I7, I12, I13, I14 (Suite VII) are comparable to M6 and M10 and more importantly are restricted to mesostructural Domain 2. They contain

abundant microfractures with dip- and strike-parallel bed-normal, or bed-parallel geometries. The strike-parallel microfractures are most common and typically have the greatest extension (Table 1), which is consistent with the geometry and extension direction of the late mesoscale veins that characterize mesostructural Domain 2. Consequently, contemporaneous deformation at two scales accommodate this dip-parallel extension.

Samples I6, I10, I11, I15 and I21 (Suite VIII) are in the most intensely deformed part of the anticline, the hinge portion of mesostructural Domain 1 with old contraction faults, young prominent solution structures, and younger contraction faults. Suite VIII is distinguished by the intensity of fracturing development, including faults (Fig. 7e, Table 1). The least deformed sample, I10, has over 5% total extension, whereas samples I6, I11 and I15 have over 15% extension. The extension in sample I21 could not be measured because two sets of FIPS arranged in arrays of en-echelon fractures darkened the thin section even at high magnifications. Also present, in samples I10 and I15, are strike-parallel, bed-normal stylolites with measured shortening strains of 5.2 and 2.8% respectively. Fracture geometries include bed-parallel and multiple bed-normal sets (Table 1), which lack consistent age relationships and in samples I6, I10 and I15 show reactivation by multiple episodes of fracturing (Figs. 7e & f). The strong fracture intensities and complex of age relationships are interpreted to indicate multiple deformation events. These events could include: (1) hinge collapse during anticlinal liftoff from the basal thrust; (2) modification of hanging wall cutoffs with the basal thrust in the NW limb causing through-hinge shear into the SE limb as possibly indicated by the presence of SE-vergent contraction faults, bedding slip surfaces through the hinge and dominant late-stage dip-parallel extension in Domain 2 and Suite VII; and (3) a late-stage layer-normal shortening event in Domain 1, which intensified into the hinge region containing Suite VIII.

Samples I8, I9, I17 and I19 (Suite IX) in the southeastern limb and mesostructural

Domain 1 contain strike-parallel, bed-perpendicular transgranular solution surfaces with a minimum volume loss of 5.0%, indicative of layer-parallel shortening. These solution structures are cut by both, strike-parallel and younger dip-parallel, bed-perpendicular microfractures with total extensions of greater than 8% except for I19. Samples I1, I2, I4, I5 and I20 (Suite X) are also in the hinge and SE limb, but are less fractured than Suite IX in terms of geometries and strains. They contain dip-parallel, bed-perpendicular microfractures with less than 1.2% extension except for I5 (4.0%). Strike-parallel, bed-normal stylolites are present in samples I5 and I20, but the volume loss due to these features is minor (<0.3%). All I-I' samples contain dip-parallel, bed-perpendicular microfractures (Table 1) unlike the O-O' profile or host syncline.

5. FINITE STRAIN ANALYSIS

Cathodoluminescence photomicrographs of each thin section were used to distinguish detrital grains from optically continuous cement overgrowths (Houseknecht 1988). Under cathodoluminescence the detrital quartz grains may be used as strain markers because their original centers can be determined (Dunne et al. 1990). The original grain boundaries of 200 quartz grains in each thin section were digitized and finite strain measured, using the normalized Fry method (Fry 1979, Erslev 1988). Strain ellipsoids were calculated from the three mutually perpendicular strain ellipses for each sample (Figs. 8, 9, Appendix B) (Owens 1984).

Host syncline

The stereonets for ellipsoid X and Y strain axes of the host syncline exhibit a weak bedding girdle (Fig. 8) that corresponds to the simple bedding girdle expected for lithification dominated by vertical compaction (Couzens et al. 1993, Couzens & Dunne 1994). This bedding girdle is also consistent with the predominance of small bedding-parallel extensions by FIPS (Table 1). Correspondingly, ellipsoidal Z strain axes cluster about the bedding normal (Fig. 8), as would be expected for pretectonic diagenetic compaction.

O-O' profile

Strain ellipsoid axes for O-O' form a similar pattern to those in the host syncline (Fig. 8) with a weak bedding-plane girdle of X and Y axes and a polar cluster of Z axes about the bedding normal. Thus, they record a compaction dominated deformation at the scale of a 200-grain region. Yet, at a slightly larger scale, the same samples record layer-parallel shortening of 2 to 3% that was accommodated heterogeneously by transgranular stylolitesand bed-parallel microfractures.

Fig. 8. Equal-area lower hemisphere stereonets depicting finite strain ellipsoid axial orientations in the host syncline, and profiles O-O', M-M' and I-I'. Bedding is restored to the horizontal to provide a common reference frame, because compaction is commonly the greatest deformation in foreland quartz arenite (Couzens et al. 1993, Couzens & Dunne 1994). The data were contoured using the Kamb (1959) method with a 3σ contour interval.

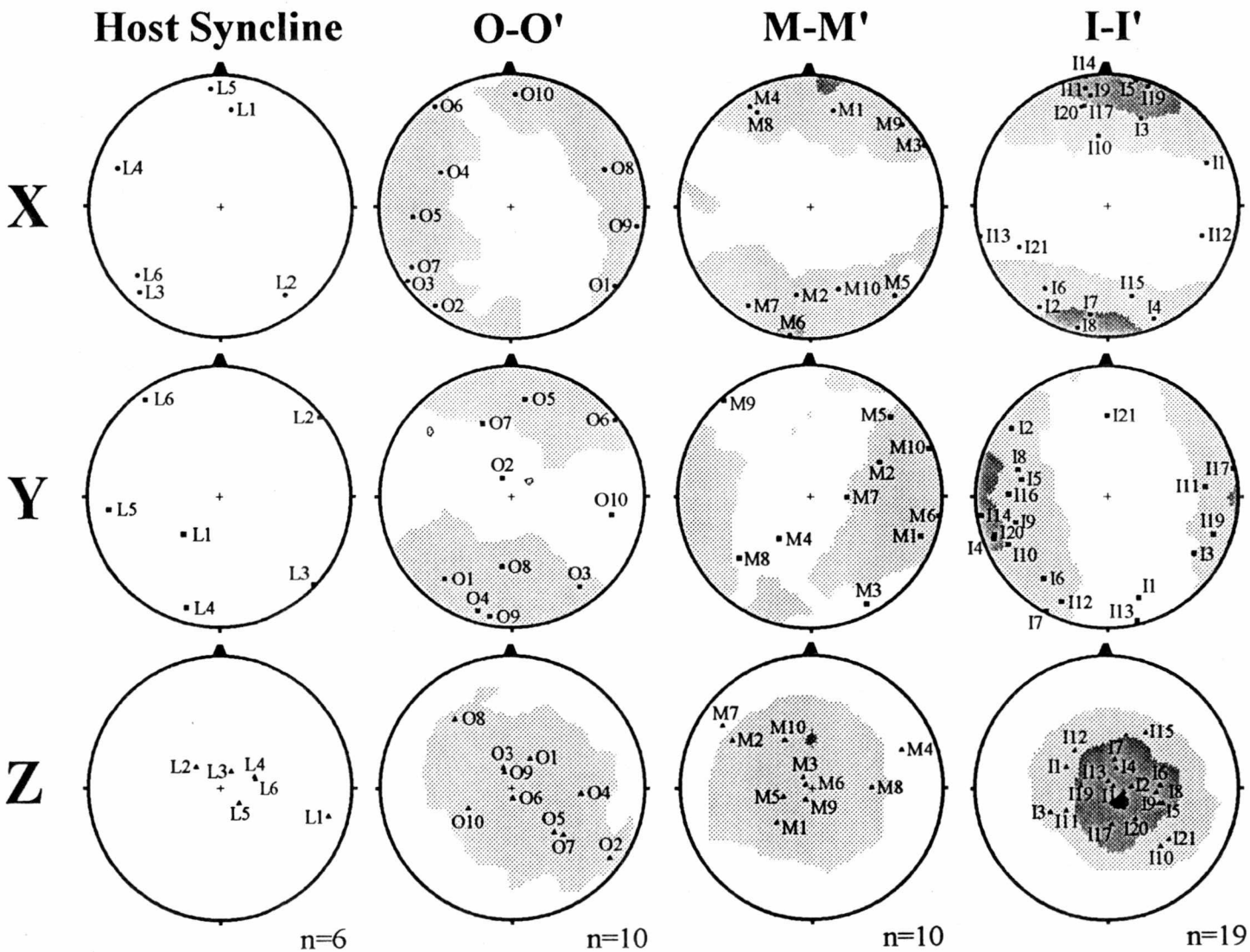
Host Syncline
O-O'
M-M'
I-I'
X
Y
Z
L5
L1
L4
L6
L3
L2
O6
O10
O8
O4
O5
O9
O7
O3
O1
O2
M4
M1
M8
M9
M3
M7
M2
M10
M5
M6
I14
I11
I9
I5
I19
I20
I17
I3
I10
I1
I13
I21
I12
I6
I15
I2
I7
I4
I8
L6
L2
L5
L1
L3
L4
O5
O7
O6
O2
O10
O1
O8
O3
O4
O9
M9
M5
M10
M2
M7
M6
M1
M4
M8
M3
I2
I21
I8
I5
I17
I16
I11
I14
I9
I19
I20
I4
I10
I3
I6
I1
I12
I13
I7
L2
L3
L4
L6
L5
L1
O8
O3
O1
O9
O6
O4
O10
O5
O7
O2
M7
M10
M2
M4
M3
M6
M5
M9
M8
M1
I12
I15
I7
I1
I13
I4
I6
I2
I8
I19
I5
I3
I11
I17
I20
I21
I10
n=6
n=10
n=10
n=19

Fig. 9. Flinn plots of finite strain data in the host syncline, and profiles O-O', M-M' and I-I'. Data points labels correspond to sample number and the plot symbol corresponds to the associated microstructural suite illustrated in Fig. 7.

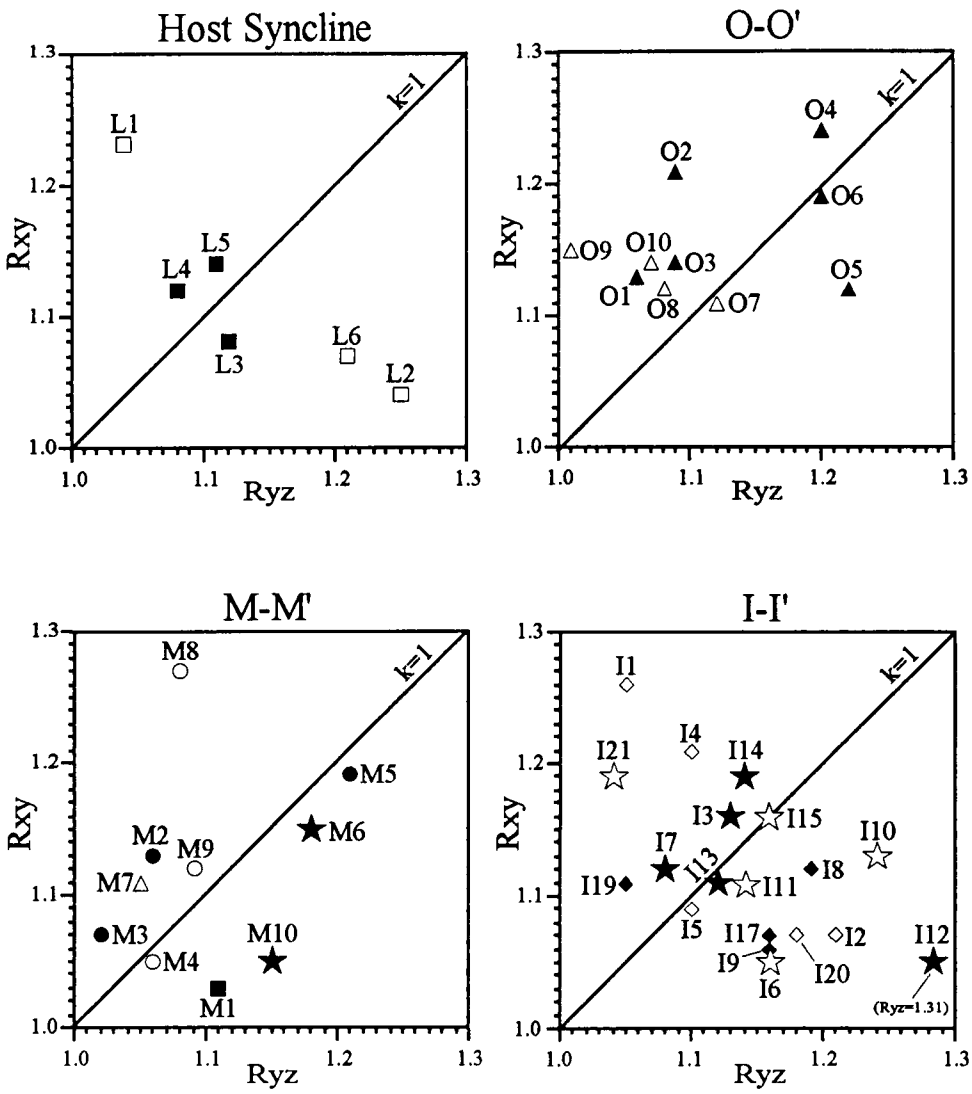
Host Syncline
k=1
L1
L5
L4
L6
L3
L2
Rxy
Ryz
1.0
1.1
1.2
1.3
O-O'
k=1
O4
O2
O6
O9
O10
O3
O5
O1
O8
O7
Rxy
Ryz
M-M'
k=1
M8
M5
M2
M9
M6
M7
M3
M10
M4
M1
Rxy
Ryz
I-I'
k=1
I1
I4
I21
I14
I3
I15
I10
I7
I13
I11
I8
I19
I5
I17
I2
I12
I9
I20
I6
(Ryz=1.31)
Rxy
Ryz

M-M' and I-I' profiles

X and Y strain ellipsoid axes from the M-M' profile have polar concentrations, N-S and E-W, respectively (Fig. 8). The polar clustering of the Z axes about the bedding normal is still present. All ellipsoidal axes in the I-I' profile have strong polar concentrations: X axes center about 010/01, Y axes center about 264/07 and Z axes center about 109/81 (Fig. 8). Such an enhanced concentration of X and Y axes as compared to samples from the host syncline and O-O' profile, is consistent with the much greater intensity of tectonic deformation at both the micro- and outcrop-scale in the I-I' samples.

6. GRAIN TO GRAIN SOLUTION

The increment of volume loss or percent shortening from grain to grain solution was determined for a representative sample set, using a new incremental strain method (PSS) (Onasch *in press*). Only 20 samples were examined because of the large time requirements for each analysis (Table 3). The method measures the volume loss by estimating the "overlap quartz" (Houseknecht 1988, Onasch *in press*) from grain interpenetration after grain-to-grain solution. The amount of interpenetration is measured as a strain from the original grain boundaries in cathodoluminescence images (Fig. 7h). The measured strains are conservative estimates because: (1) measurements are only made where grains clearly indented other grains, so that straight boundaries with potentially significant solution are not used; (2) indenters may have their amplitude reduced during solution, but this effect is not included in the method; and (3) only the interactions between original grains are examined so that solution of diagenetic cements would be unmeasured.

As with the finite strain data, strain ellipses for the PSS data were measured in three mutually perpendicular planes (Table 3) and ellipsoids were calculated from the ellipses (Appendix C) (Owens 1984). The PSS strain data indicate area loss of about 28% per thin section (Table 3), and volume loss per sample of about 39% by solution. The average preserved diagenetic cement of 4.6% (Table 4) is consistent with this volume loss by grain to grain solution. Such a cement content would indicate a porosity loss of 35% for well sorted quartz sands that commonly having initial porosities of about 40% (Beard & Weyl 1973, Pettijohn et al. 1987, Houseknecht 1988) and formed the Keefer Sandstone.

The volume loss appears to be triaxial because all axes have absolute magnitudes of <1.0 (Table 3). When two or more shortening directions occur during volume-loss deformation, they are difficult to determine from the PSS data because grain overlaps from volume loss in one direction create an apparent strain when viewed in other directions

Table 3. Strain ellipses measured with PSS method.

		b-section					p-section					v-section				
Sample	Suite	Long Axis	Short Axis	Axial Ratio	Axial Rake	% Area Loss	Long Axis	Short Axis	Axial Ratio	Axial Rake	% Area Loss	Long Axis	Short Axis	Axial Ratio	Axial Rake	% Area Loss
L1	II	0.90	0.81	1.11	0	27	0.90	0.83	1.08	0	25	0.83	0.81	1.02	0	33
L2	II	0.89	0.83	1.07	0	26	0.88	0.80	1.10	0	30	0.83	0.81	1.02	0	33
L3	I	0.84	0.75	1.12	0	37	0.86	0.82	1.05	0	29	0.82	0.80	1.03	90	34
O2	III	0.85	0.82	1.04	0	30	0.85	0.80	1.06	0	32	0.85	0.84	1.01	0	29
O3	III	0.83	0.81	1.02	90	33	0.87	0.76	1.14	0	34	0.84	0.76	1.11	0	36
O5	III	0.85	0.82	1.04	0	30	0.85	0.85	1.00	0	28	0.86	0.82	1.05	0	29
O6	III	0.86	0.85	1.01	0	27	0.85	0.83	1.02	0	29	0.88	0.83	1.06	0	27
O9	IV	0.88	0.86	1.02	0	24	0.87	0.85	1.02	0	26	0.90	0.85	1.06	0	24
M1	I	0.89	0.83	1.07	0	26	0.87	0.82	1.06	0	29	0.89	0.83	1.07	0	26
M2	V	0.91	0.85	1.07	0	23	0.91	0.83	1.10	0	24	0.86	0.83	1.04	0	29
M3	V	0.93	0.90	1.03	0	16	0.93	0.83	1.12	0	23	0.90	0.84	1.07	0	24
I4	X	0.87	0.85	1.02	0	26	0.88	0.85	1.04	0	25	0.85	0.85	1.00	0	28
I6	VIII	0.90	0.86	1.05	0	23	0.89	0.84	1.06	0	25	0.91	0.86	1.06	-31	22
I9	IX	0.88	0.83	1.06	0	27	0.91	0.83	1.10	0	24	0.92	0.85	1.08	-24	22
I10	VIII	0.90	0.85	1.06	0	24	0.88	0.85	1.04	0	25	0.90	0.85	1.06	-27	24
I11	VIII	0.91	0.84	1.08	-16	24	0.91	0.85	1.07	0	23	0.90	0.85	1.06	-23	24
I12	VII	0.89	0.83	1.07	0	26	0.87	0.82	1.06	0	29	0.89	0.83	1.07	0	26
I13	VII	0.90	0.85	1.06	0	24	0.87	0.84	1.04	-28	27	0.88	0.82	1.07	0	28
I14	VII	0.88	0.82	1.07	0	28	0.90	0.84	1.07	0	24	0.85	0.84	1.01	0	29
I19	IX	0.85	0.82	1.04	0	30	0.85	0.83	1.02	0	29	0.87	0.81	1.07	0	30
I20	X	0.83	0.82	1.01	0	32	0.82	0.81	1.01	0	34	0.84	0.82	1.02	0	31

Rake measured in the plane of bedding with strike as a common reference frame.

Table 4. Percentage of silica cement in quartz arenite samples.

Sample	b-section	v-section
L1	3.0	2.5
L2	3.0	3.5
L3	5.0	4.0
L4	3.5	2.5
L5	4.0	0.0
L6	2.5	2.5
O1	2.0	4.0
O2	6.0	7.5
O3	5.5	4.0
O4	3.5	2.0
O5	5.0	4.5
O6	3.5	6.0
O7	4.0	3.5
O8	5.5	1.5
O9	5.5	3.0
O10	2.5	3.0
M1	8.5	5.0
M2	7.5	9.0
M3	9.0	7.5
M4	5.0	5.0
M5	0.5	2.5
M6	7.0	5.0
M7	4.5	4.5
M8	6.0	5.5
M9	4.5	3.0
M10	4.0	6.5
I1	4.5	5.0
I2	3.0	4.0
I3	6.0	3.5
I4	3.5	7.0
I5	5.0	3.0
I6	6.0	3.5
I7	5.0	3.0
I8	n/a	n/a
I9	7.5	5.5
I10	4.5	4.0
I11	4.0	6.0
I12	4.0	3.0
I13	2.5	4.5
I14	5.5	5.5
I15	8.5	7.5
I17	5.5	7.0
I19	n/m	n/m
I20	n/m	n/m
I21	n/m	n/m

n/a -not applicible; n/m -not measured

(Onasch *in press*). This effect is easy to isolate for single uniaxial volume losses (Onasch *in press*, Onasch pers. comm.), but is more problematic for several events with different shortening directions. Still, the strain ellipses for the PSS data consistently show layer-normal-dominated volume loss in the bed-normal p- and v-sections because long axes are in the plane of bedding (rake=0). They also reveal strike-normal layer-parallel shortening by volume loss in the bedding plane (b sections) because the long axes are consistently parallel to strike (rake=0). These geometries are probably indicative of the importance of the two deformation events of diagenetic compaction and LPS for the grain-to-grain solution strains.

The ellipsoidal axes (Fig. 10) have very similar distributions to the axes from the finite strain data (Fig. 8). The samples from the host syncline, O-O' and M-M' have most X and Y axes in the bedding plane girdles with Z axes normal to bedding. I-I' samples produce strong polar concentrations in bedding for both X and Y axes (Fig. 10).

Implications for deformation behavior of the quartz arenite

The finite and grain-to-grain solution strains were measured in domains that contain 200 grains and the microstructures that caused the strains must be present within these domains. Intragranular microstructures related to dislocation movements are one possibility for producing the strains. Point counts for the abundance of these microstructures however, eliminates subgrains, deformation lamellae and deformation bands from consideration because they are virtually absent (Table 2). Also, features such as mortar texture and FRAIS are indicative of fracturing and not the movement of dislocations. Although, simple undulatory extinction is abundant (Table 2), this microstructure may be inherited from the sedimentary source rock (Onasch & Dunne 1993). Given this possibility, the undulatory extinction probably only accounts for a very small tectonic strain increment at best because of the rare occurrence of the other

Fig. 10. Equal-area lower hemisphere stereonets depicting PSS incremental strain ellipsoid axial orientations for the host syncline, and profiles O-O', M-M' and I-I'. Bedding is restored to the horizontal in order to provide a common reference frame. Axial orientations are listed in Table 3. X-axes are represented by white circles, Y-axes by white squares and Z-axes by white triangles. Symbol overlaps are marked on the stereonets.

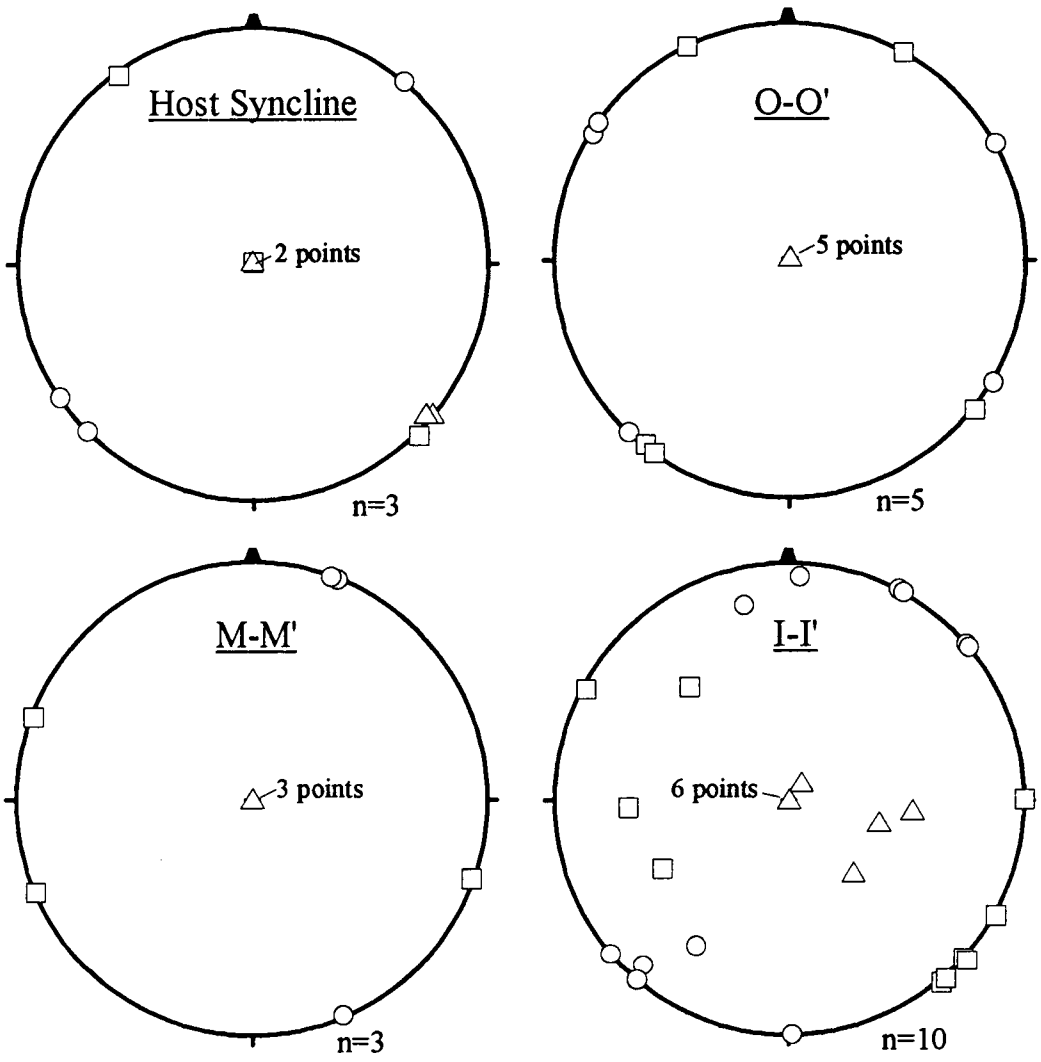
Host Syncline
2 points
n=3
O-O'
5 points
n=5
M-M'
3 points
n=3
I-I'
6 points
n=10

dislocation-related microstructures. Consequently, intragranular deformation was not a primary contributor to the measured finite strains.

Other possible microstructures with measurable strains such as transgranular solution surfaces and microveins (Table 1) are eliminated from consideration because the 200-grain domains were selected to avoid these discontinuous features and to preserve homogeneity of deformation. FIPS and grain-to-grain solution features are the only other observed microstructures to account for the finite strains in these domains. As previously noted, the bedding-normal geometry of most FIPS in the host syncline is consistent with the X and Y axial girdles. Yet, the wall-normal extensions of the FIPS never exceed 2.5% and commonly are less than 0.6% (Table 1). These small strains are insufficient to account for finite strain ratios of 1.1 to 1.3 (Fig. 9). In contrast, the grain-to-grain solution strains are much larger (Table 3), but they have two problematic characteristics with respect to the finite strains: (1) grain-to-grain strain ratios are consistently smaller (Fig. 9, Table 3); and (2) they have nearly perfect bed-normal polar concentrations of Z-axes with nearly perfect bedding-plane girdles for the X and Y axes in contrast to the greater diversity of orientations for the finite strain axes (Figs. 8, 10).

The first problem could simply be an artifact of the PSS method underestimating total grain-to-grain solution shortening, particularly due to the abundance of straight grain boundaries. The second problem requires another deformation mechanism or textural characteristic at the scale of the 200-grain domains to cause a difference in the axial diversity between the grain-to-grain solution and finite strains. The possible deformation mechanisms would have no microstructural imprint because we have accounted for all microstructures (Fig. 5, Tables 1, 2). The deformation mechanism that may have this attribute is grain-boundary sliding, which only changes nearest-neighbor arrangements by rigid-body translation (Maltman 1984, Owen 1987, Groshong 1988, Knipe 1989). Still, grain-boundary sliding in a tightly cemented quartz arenite should require additional

deformation mechanisms such as cataclasis or solution to enable grains to move with respect to each other. Cataclasis is virtually absent in the samples (Fig. 7, Table 1). Solution is already identified, measured, and did not produce diverse axial orientations (Fig. 9), therefore grain-boundary sliding did not have a significant role during deformation of this quartz arenite. Thus, unseen deformation mechanisms did not cause the difference in axial concentrations between grain-to-grain solution and finite strains. Instead, the difference must result from an intrinsic textural characteristic of the grain population as recorded by only one of the two strain measurement techniques. We propose that this intrinsic characteristic is the depositional grain fabric as recorded by the spatial measurements of the normalized Fry method for the finite strains. These framework-supported sandstones meet the requirement for this type of strain measurement by preserving nearest-neighbor relationships during deformation. Yet, we suggest that depositional grain clustering from grain size variation and changes in packing (Crespi 1986) is not completely eliminated by the normalization procedure (Erslev 1988), particularly for small strains as measured in this study (Fig. 9). Variation in this depositional fabric from sample to sample could produce the axial diversity of the finite strain measurements, but would not influence the incremental strains as measured from grain interpenetrations for the PSS method.

Assuming this proposition is correct, the majority of the homogeneous grain-scale deformation in this quartz arenite was by grain-to-grain solution with minor contributions from the formation of FIPS and dislocation-related microstructures (Figs. 8, 10, Tables 1, 2, 3). Significant heterogeneous strain at a slightly larger scale was accommodated by the formation of microveins and transgranular solution surfaces (Figs. 5, 7, Table 1). This heterogeneity of deformation is also characteristic of later mesoscale structural development, particularly during the formation of the late-stage mesostructural Domains 1 and 2 in the I-I' profile (Fig. 5). The sequence of deformation mechanisms and their

spatial distribution indicates both an increase in the size of the resulting structures and an increase in strain heterogeneity with progressive deformation from compaction to the completion of folding. This sequence of behavior may reflect the change from a porous sand to a tightly cemented sandstone where the lose of porosity precluded pervasive transgranular deformation, and the relatively low temperature/pressure conditions precluded pervasive intragranular deformation.

The proposed suite of deformation mechanisms at the micro- and mesoscales developed in temperature conditions of 165° C to 285° C for 6 to 9 km of burial at a 25° to 30° C km^{-1} geothermal gradient with a lithostatic load of about 150 to 225 MPa (Colton 1970, Epstein et al. 1977, Onasch & Dunne 1993, Zhang & Davis 1993). These microstructures, which are dominated by solution and fractures, and deformation conditions are similar to those reported for sandstone deformation by Onasch & Dunne (1993) and Wu & Groshong (1991). The only significant difference of these results to the previous work is the attribution of mortar textures to fracture rather than dislocation movement (Wu & Groshong 1991).

Volume loss

The average volume loss of 39% from PSS measurements is greater than the combined porosity of the rock (<<1%), the amount of preserved diagenetic cement (averaging 4.6% per sample, Table 4), and volume increases related to dilations from FIPS and microvein formation (commonly total ≤8% and never >19.9% (Table 1)). Consequently, the Keefer Sandstone underwent net volume loss during lithification and subsequent tectonic events.

The geometries of the strain ellipses and ellipsoids for the PSS method (Fig. 10, Table 3) indicate two prominent events during deformation: layer-normal volume loss during compaction and strike-normal, layer-parallel shortening during tectonic

deformation. The compaction produced greater volume loss because ellipsoidal Z axes are normal to bedding, whereas the layer-parallel shortening was insufficient to concentrate a compaction-generated bedding girdle of X axes into a polar concentration that is parallel to strike except for I-I' samples. This proposed layer-parallel shortening is consistent with the presence of strike-parallel, bed-normal transgranular stylolites in some samples (Table 1).

I-I' also contains the only data set where clear structural evidence exists at both the meso- and microscale for a post-compactional volume-loss event, the late-stage layer-normal shortening in mesostructural Domain 1. At the microscale, this event caused a greater diversity of Z axes with respect to bedding in both the PSS and finite strain data (Figs. 8, 10, Table 3) for samples mainly from microstructural Suite VIII. This diversity may be indicative of heterogeneous deformation concentrated along a few grain contacts, which would be consistent with the intense concentration of solution at the mesoscale along contraction faults and bedding surfaces. Certainly, even if fluids pervaded the limited grain-scale porosity during this deformation, they caused much more deformation along the mesoscale discontinuities.

7. FOLD DEVELOPMENT

The oldest deformation of the Keefer Sandstone is diagenetic compaction that was dominated by grain to grain solution. This event produced the greatest strain increment and caused a strong bedding-normal concentration of finite strain ellipsoidal Z axes (Fig. 8). Layer-parallel shortening (LPS) followed compaction, most likely the response to Alleghanian cover deformation above a blind duplex (Ferrill & Dunne 1989). The contribution of LPS to the finite strain data is minor as compared to diagenetic compaction because Z axes are bed-normal and not bed-parallel, and X axes only deviate from a compactional bedding girdle distribution for samples from the I-I' profile where tectonic deformation was most intense (Figs. 8, 10).

LPS in the stiff layers was followed by buckle folding that was contemporaneous with additional LPS in less stiff units (Ferrill & Dunne 1989). The Keefer Sandstone folded in at least two scales, the host syncline and parasitic target anticline. Buckling rotated and steepened the host syncline limbs, produced a NW vergence with a more steeply dipping southeast limb and resulted in the formation of numerous mechanical layers as evidenced by abundant dip- and layer-parallel slip-surfaces. The limbs only contained microstructural evidence for grain to grain solution except where limb dips steepened and the outcrop of the syncline narrowed. There, meso- and microscale veins developed to accommodate predominantly dip-parallel, layer-parallel extension, perhaps in response to subhorizontal compression of subvertical beds

Development of the parasitic anticline

Assuming the O-O' profile near the anticlinal termination to be the youngest portion of the fold, the fold amplified with a northwest-verging shape. During amplification, layer-parallel slip occurred in the limbs and through the hinge, and tangential longitudinal strain as marked by strike-parallel veins developed in the hinge (Fig. 5b, Table

1). Within the profile, LPS was enhanced prior to or during folding by the development of bedding-normal stylolites and bed-parallel FIPS. This deformation was heterogeneous at the scale of the 200-grain domains for strain measurement, but ubiquitous at the scale of the fold (Fig. 5b, Table 1). If space can be traded for time when examining the deformation history of the anticline, this relatively simple structural suite and deformation sequence should be present in the M-M' profile as older structures and events.

Only the lower layers in M-M' may be used for comparison because contraction faults with bedding-parallel slip have displaced rocks from the southeastern limb into the hinge in the upper part of the fold. Comparing profiles, M-M' is tighter (79° vs. 113°), broader in arc length (4.25 m vs. 2.0 m), and has less hinge curvature (28.5°/m vs. 33.5° /m) than O-O'. If O-O' was a precursor form to the profile at M-M', the fold hinge must have broadened and reduced curvature during amplification. The micro/mesostructural imprint from this event and the precursor events as found in O-O' are missing from M-M'. First, M-M' in all hinge samples (M3, M4, M5, M8, M9 in Table 1, Figs. 5b & c) lacks relict veins from outer-arc extension that accommodated 5% extension in the hinge during folding of O-O'. Secondly, the hinge zone in M-M' lacks the layer-parallel shortening structures that would be necessary to accommodate the decrease in curvature during amplification from the hinge shape of O-O' to M-M'. Additionally, M-M' lacks the microstructures of transgranular stylolites and bed-parallel FIPS that recorded an additional increment of LPS in O-O'. Consequently, the microstructural evidence indicates that despite sharing a similar NW-verging fold shape, the deformation at O-O' was not like the initial deformation at M-M'. Space may not be traded for time when comparing O-O' to M-M'.

The I-I' hinge may not be compared directly to M-M' or O-O' hinges because it represents a second anticlinal hinge emplaced on the first anticline as a thrust-related fold. Still, the rocks of I-I' are laterally equivalent to rocks in the SE limb of O-O'. I-I' does not

contain the intensification of LPS by transgranular stylolites and FIPS that is present in all samples from the SE limb of O-O'. Again, microstructural evidence indicates that space may not be traded for time.

Although no direct relationship between space and time could be found for the deformation history of this fold, the approach that space can be traded for time is perhaps still applicable to other structures. Certainly, this fold is not representative of all geologic structures. Possible reasons as to why space could not be traded for time in this fold perhaps involve the effects of changing conditions along the fold hinge or a change in fold mechanisms from profile to profile, as indicated by the contraction faults in M-M' and I-I' (Fig. 5). Additionally, it is arguable that the fold defined by O-O' and M-M' is actually thrust-related rather than the result of simple buckling because of the steeper dips in the NW limb and the close proximity of O-O' to the NW limb of the host syncline (Figs. 3, 4). If O-O' and M-M' are part of a thrust-related anticline, the test of "trading space for time" is still appropriate because the concept is used for both buckle and thrust-related folds. Field evidence for a thrust fault between O-O' and the host syncline is lacking, however, and based on the common occurrence of buckle folds in the Keefer Sandstone of eastern West Virginia (Lessing 1987, Figs. 19, 20 in Lessing et. al 1991), we believe the fold is primarily the result of buckling rather than thrusting.

The three profiles do share three similarities: (1) a NW-verging asymmetric fold shape; (2) bedding-parallel slip surfaces indicative of layer-slip during fold growth; and (3) a late-stage set of vertical, 110° to 120° trending white "hairline" veins that accommodated an axial extension of $\leq 0.3\%$. For profiles O-O' and M-M', the asymmetric shape may be indicative of an initial asymmetric perturbation (Chapple & Spang 1974, Abbassi & Mancktelow 1990), but in I-I' the asymmetry results from being thrust-related.

Grossly, anticlinal development had some similarity along its length, even where complicated by the formation of a second thrust-related hinge. The fold preferentially

rotated the NW limb, developed with the aid of bedding slip and experienced a minor late-stage axial extension. Despite these similarities, fold growth differed significantly in detail from point to point along the fold axis, precluding the analytical approach of "trading space for time" when examining the deformation history. Any profile across the fold has to be examined separately to determine the local sequence of limb rotation, hinge bending, layer-parallel shear strain or slip, or faulting.

8. CONCLUSIONS

(1) Fold growth was grossly similar along the hinge of the anticline from culmination to termination with a NW-vergence, straight limbs and curved hinge, and folding by layer-parallel slip. However, the microstructural, mesostructural and strain distributions at the termination are not found in the culmination, even as the oldest structures. Therefore, "space may not be traded for time" when analyzing the three-dimensional deformation history of this fold. Given the similar results for a thrust-related anticline at map scale (Fischer & Woodward 1990), we believe that the deformation history in a given profile across a fold is generally dependent on local parameters and will not mimic the earlier deformation history in older portions of the fold. Although the behavior of "trading space for time" is not applicable to this fold, more tests for this behavior should be pursued and documented. We advise, however, that this approach of "trading space for time" in the analysis of folds and other structures be used with caution.

(2) The quartz arenite of the Keefer Sandstone was most deformed internally during lithostatic compaction by grain-to-grain solution. Additional grain-to-grain solution occurred during LPS with localized deformation by the formation of bed-normal transgranular stylolites and bed-parallel FIPS. All subsequent deformations developed in response to local conditions in the fold, produced discontinuous structures such as microveins, faults, and pressure-solution surfaces, and were heterogeneous distributed at the grain scale. Progressive deformation was marked by a transition from pervasive to discontinuous at the grain scale as a function of lost porosity and insufficient temperatures.

(3) The finite strains record a much more diverse distribution of axial orientations than the ellipsoidal strain axes for the largest strain increment due to grain-to-grain solution. This difference in the geometry of strain axes is interpreted to result from the original grain distribution and not the activity of other deformation mechanisms such as grain-boundary sliding.

REFERENCES

REFERENCES

Abbassi M. R. & Mancktelow, N. S. 1990. The effect of initial perturbation shape and symmetry on fold development. *J. Struct. Geol.* **12**, 273-282.

Bamford, M. L. F. & Ford, M. 1990. Flexural shear in a periclinal fold from the Irish Variscides. *J. Struct. Geol.* **12**, 59-68.

Beard, D. C. & Weyl, P. K. 1973. Influence of texture on porosity and permeability of unconsolidated sand. *Bull. geol. Ass. Petrol. Geol.* **57**, 349-369.

Chapple, W. M. & Spang, J. H. 1974. Significance of layer-parallel slip during folding of layered sedimentary rocks. *Bull. geol. Soc. Am.* **85**, 1523-1534.

Colton, G. W. 1970. The Appalachian basin--its depositional sequences and their geologic relationships. In: Studies of Appalachian Geology: Central and Southern, eds. Fischer, G. W., Pettijohn, F. J., Read, J. C, Jr. & Weaver, K. N.. New York, Wiley-Interscience.

Couzens, B. A., Dunne, W. M., Onasch, C. M. & Glass R. 1993. Strain variations and three-dimensional strain factorization at the transition from the southern to central Appalachians. *J. Struct. Geol.* **15**, 451-464.

Couzens, B. A. & Dunne, W. M. 1994. Displacement transfer at thrust terminations: The Saltville thrust and Sinking Creek anticline, Virginia, U.S.A.. *J. Struct. Geol.*

Crespi, J. M. 1986. Some guidelines for the practical applications of Fry's method of strain analysis. *J. Struct. Geol.* **8**, 799-808.

Dubey, A. K. & Cobbold, P. R. 1977. Noncylindrical flexural slip folds in nature and experiment. *Tectonophysics* **38**, 223-239.

Dunne, W. M., Onasch, C. M. & Williams, R. T. 1990. The problem of strain marker centers and the Fry method. *J. Struct. Geol.* **12**, 933-938.

Epstein, A. G., Epstein, J. B. & Harris, L. D. 1977. Conodont color alteration—an index to organic metamorphism. *Prof. Pap. U.S. geol. Surv*, **995**.

Erslev, E. A. 1988. Normalized center-to-center strain analysis of packed aggregates. *J. Struc.Geol.* **10**, 201-210.

Ferrill, D. A. & Dunne, W. M. 1989. Cover deformation above a blind duplex: an example from West Virginia, U.S.A.. *J. Struct. Geol.* **11**, 421-431.

Fischer, M. P. & Woodward, N. B. 1990. *The geometric evolution of foreland thrust systems: Thrust tectonics,* ed. McClay, K. R., London, Chapman and Hall.

Folk, R. L. 1960. Petrography and origin of the Tuscarora, Rose Hill and Keefer Formations, Lower and Middle Silurian of eastern West Virginia. *J. Sedim. Petrol.* **30**, 1-58.

Fry, N. 1979. Random point distributions and strain measurements in rocks. *Tectonophysics* **60**, 89-105.

Groshong Jr., R. H. 1975. Strain, fractures, and pressure solution in natural single-layer folds. *Bull. geol. Soc. Am.* **86**, 1363-1376.

Groshong Jr., R. H. 1988. Low-temperature deformation mechanisms and their interpretations. *Bull. geol. Soc. Am.* **100**, 2025-2038.

Gwinn, V. E. 1964. Thin-skinned tectonics in the Plateau and northwestern Valley and Ridge province of the central Appalachians. *Bull. geol. Soc. Am.* **75**, 863-900.

Heald, M. T. 1955. Stylolites in sandstones. *J. Geol.* **63**, 101-114

Hobbs, B. E., Means, W. D. & Williams, P. F. 1976. *An outline of structural geology.* New York, John Wiley & Sons, Inc.

Houseknecht, D. W. 1988. Intergranular pressure solution in four quartzose sandstones. *J. sedim. Petrol.* **58**, 228-246.

Kamb, W. B. 1959. Ice petrofabric observations from Blue Glacier, Washington, in relation to theory and experiment. *J. geophys. Res.* **64**, 1891-1909.

Knipe, R. J. 1989. Deformation mechanisms--recognition from natural tectonites. *J. Struct. Geol.* **11**, 127-146.

Kulander, B. R. & Dean, S. L. 1986. Structure and tectonics of the southern and central Appalachian Valley and Ridge and Plateau provinces, West Virginia and Virginia. *Bull. Am. Ass. Petrol. Geol.*, **70**, 1674-1684.

Lessing, P., Dean, S. L. & Kulander, B. R. 1991. Stratigraphy and structure of the Great Valley and Valley and Ridge, West Virginia. In: Geologic evolution of the eastern United States. Field trip guidebook NE-SE 1991, eds. Schultz, A. & Compton-Gooding, E.. Martinsville, Virginia, Virginia Museum of Natural History.

Lessing, P. 1987. Fluted Rocks—A magnificent exposure to the forces of Mother Nature. *Mountain State Geol., W. Va. geol. Surv.*,20-28.

Maltman, A. 1984. On the term 'soft sediment' deformation. *J Struct. Geol.* **6**, 589-592

Namson, J. 1981. Structure of the western foothills belt, Miaoli-Hsinchu area, Taiwan: (I) Southern part. *Petrol. Geol. Taiwan* **19**, 31-51.

Narahara, D. H. & Wiltschko D. V. 1986. Deformation in the hinge region of a chevron fold, Valley and Ridge Province, central Pennsylvania. *J. Struct. Geol.* **8**, 152-168.

Nickelsen, R. P. 1979. Sequence of structural stages of the Alleghany Orogeny, at the Bear Valley Strip Mine, Shamokin, Pennsylvania. *Am. J. Sci.* **279**, 225-271.

Onasch, C. M. 1990. Microfractures and their role in deformation of a quartz arenite from the central Appalachian foreland. *J. Struct. Geol.* **12**, 883-894.

Onasch, C. M. & Dunne, W. M. 1993. Variation in quartz arenite deformation mechanisms between a roof sequence and duplexes. *J. Struct. Geol.* **15**, 465-475.

Onasch, C. M. In press. Determination of pressure solution shortening in sandstones. *Tectonophysics.*

Owen, G. 1987. Deformation processes in unconsolidated sands. In: *Deformation of Sediments and Sedimentary Rocks*, eds. Jones, M. E. & Preston, R.. *Spec. Publs. geol. Soc. Lond.* **29**, 11-24.

Owens, W. H. 1984. The calculation of a best fit ellipsoid from elliptical sections on arbitrarily oriented planes. *J. Struct. Geol.* **6**, 571-577.

Perry, W. J. 1978. Sequential deformation in the central Appalachians. *Am. J. Sci.* **278**, 518-542.

Pettijohn, F. J., Potter, P. E. & Siever, R. 1987. *Sand and Sandstone.* New York. Springer-Verlag.

Ramberg, H. 1964. Selective buckling of composite layers with contrasted rheological properties; a theory for simultaneous formations of several orders of folds. *Tectonophysics* **1**, 307-341.

Rodgers, J. 1970. *The tectonics of the Appalachians.* New York, Wiley-Interscience.

Stewart, K. G. & Alvarez, W. 1991. Mobile-hinge kinking in layered rocks and models. *J. Struct. Geol.* **13**, 243-259.

Stockdale, P. B. 1926. The stratigraphic significance of solution in rocks. *J. Geol.* **34**, 399-414.

Suppe, J. 1983. Geometry and kinematics of fault-bend folding. *Am. J. Sci.* **283**, 684-721.

Suppe, J. & Medwedeff, D. A. 1990. Geometry and kinematics of fault-propagation folding. *Ecologae Geol. Helvetiae* **83**, 409-454.

Tada, R. & Siever, R. 1989. Pressure solution during diagenesis. *Ann. Rev. Earth Planet. Sci.* **17**, 89-118.

Tilton, J. L., Prouty, W. F., Tucker, R. C. & Price, P. H. 1927. Hampshire and Hardy counties. West Virginia Geological Survey, Morgantown, West Virginia, Morgantown Printing and Binding Company.

Wu, S. & Groshong Jr., R. H. 1991. Low-temperature deformation of sandstone, southern Appalachian fold-thrust belt. *Bull. geol. Soc. Am.* **103**, 861-875.

Zhang, E. & Davis, A. 1993. Coalification patterns of the Pennsylvanian coal measures in the Appalachian foreland basin, western and south-central Pennsylvania. *Bull. geol. Soc. Am.* **105**, 162-174.

APPENDIXES

APPENDIX A: ORIENTATION DATA, SAMPLE PREPARATION AND DATA COLLECTION

This first part of this appendix contains field data (strike and dips) collected at all the sample and station locales (Table A.1). An exposure map dipicting sample and station locations is included (Fig. A.1). Fold axial trends and plunges for the Host syncline and each profile were determined using all data relavant to the particular field location in question. Steronet© by R. W. Allmendinger for the Macintosh© was used to process the orientation data.

The second section of Appendix A outlines and shematically demonstrates the procedures taken for thin-section preparation and strain data collection.

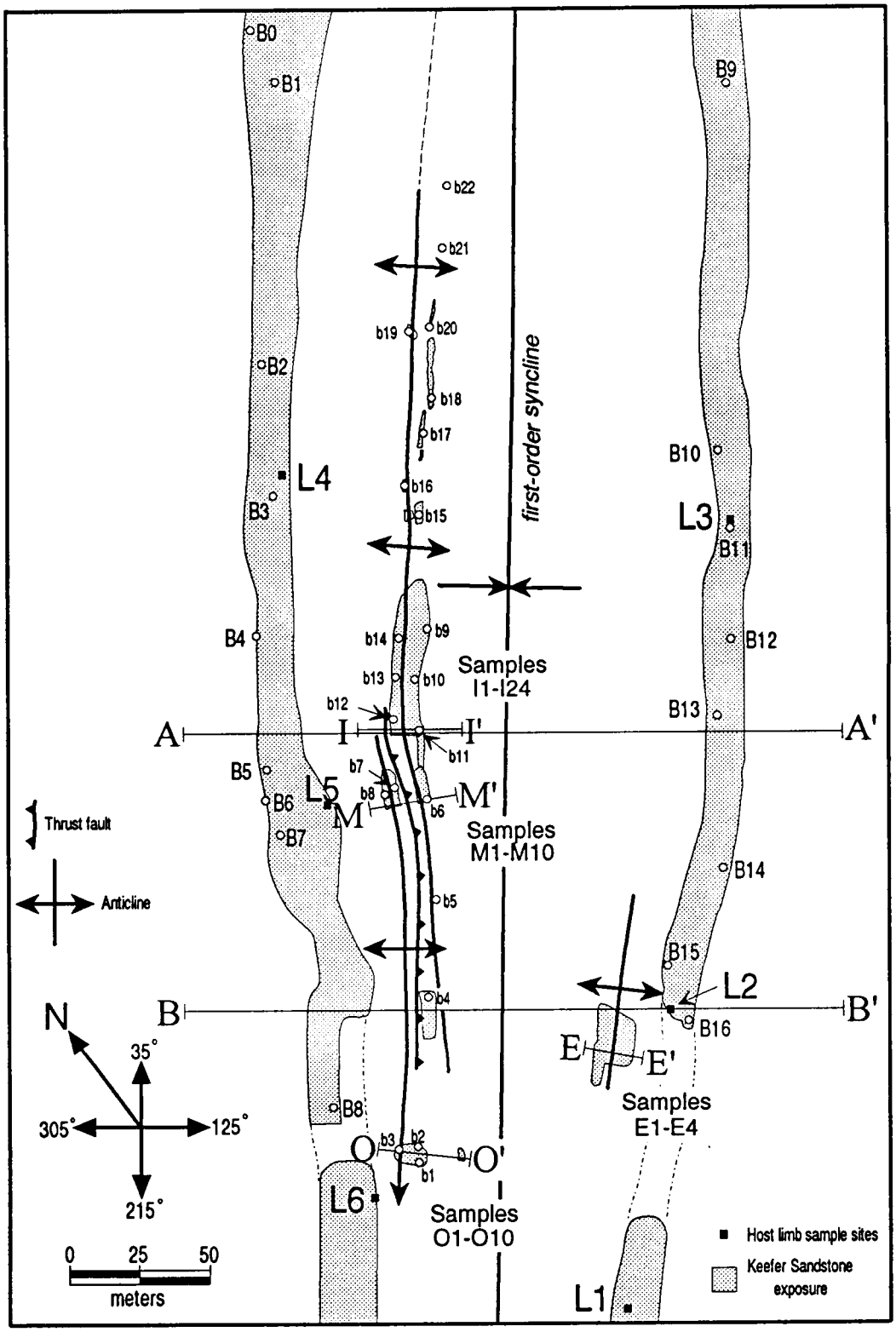

Fig. A.1. Keefer Sandstone exposure map showing sample and station locations.

Table A.1. Bedding orientations of samples.

Field Location	Sample number	Strike/Dip	Quad.	
	L1	045/87	NW	
	L2	055/89	NW	
Host	L3	040/68	NW	Trend: 222
Syncline	L4	045/50	SE	Plunge: 02
	L5	035/50	SE	
	L6	041/62	SE	
	O1	052/24	SE	
	O2	065/22	S	
	O3	032/18	SE	
	O4	039/17	SE	
O-O'	O5	039/20	SE	Trend: 216
Profile	O6	035/10	SE	Plunge: 03
	O7	033/02	SE	
	O8	034/08	NW	
	O9	032/34	NW	
	O10	031/40	NW	
	M1	337/17	SW	
	M2	020/42	W	
	M3	021/43	W	
	M4	030/67	NW	
M-M'	M5	012/41	W	Trend: 204
Profile	M6	041/38	SE	Plunge: 02
	M7	024/20	E	
	M8	011/03	SE	
	M9	012/01	SE	
	M10	021/34	SE	
	I1	037/25	SE	
	I2	019/65	SE	
	I3	034/86	SE	
	I4	029/61	SE	
	I5	028/72	SE	
	I6	049/03	SE	
	I7	043/86	SE	
	I8	012/64	SE	
	I9	028/52	SE	
	I10	031/69	SE	
	I11	034/58	SE	
I-I'	I12	040/81	SE	Trend: 033
Profile	I13	041/67	NW	Plunge: 01
	I14	036/67	NW	
	I15	049/67	NW	
	I16	043/43	SE	
	I17	013/72	SE	
	I18	050/28	SE	
	I19	040/10	SE	
	I20	050/15	SE	
	I21	035/20	SE	
	I22	120/4	NW	
	I23	035/20	NW	
	I24	045/15	NW	
	E1	021/37	E	
Parasitic	E2	032/35	NW	Trend: 034
Anticline	E3	042/45	NW	Plunge: 03
	E4	038/28	SE	

Table A.1. continued... (station data)

Station number	Strike/Dip	Quad.	Location
B0	045/48	SE	Host syncline
B1	038/42	SE	Host syncline
B2	056/46	SE	Host syncline
B3	040/42	SE	Host syncline
B4	038/44	SE	Host syncline
B5	051/48	SE	Host syncline
B6	041/46	SE	Host syncline
B7	040/42	SE	Host syncline
B8	042/60	SE	Host syncline
B9	027/38	NW	Host syncline
B10	037/41	NW	Host syncline
B11	050/16	NW	Host syncline
B12	040/60	NW	Host syncline
B13	034/70	NW	Host syncline
B14	036/72	NW	Host syncline
B15	051/82	NW	Host syncline
B16	041/88	SE	Host syncline
b1	047/17	SE	O-O'
b2	045/18	SE	O-O'
b3	020/18	NW	O-O'
b4	016/51	W	Fold Axis
b5	034/56	SE	Fold Axis
b6	023/87	SE	M-M'
b7	014/34	E	M-M'
b8	026/42	NW	M-M'
b9	032/76	SE	I-I'
b10	032/54	SE	I-I'
b11	032/78	SE	I-I'
b12	034/82	NW	I-I'
b13	040/56	NW	I-I'
b14	029/52	NW	I-I'
b15	026/36	SE	Fold Axis
b16	046/06	NW	Fold Axis
b17	048/57	SE	Fold Axis
b18	049/54	SE	Fold Axis
b19	021/60	NW	Fold Axis
b20	034/58	SE	Fold Axis
b21	039/86	SE	Fold Axis
b22	041/80	SE	Fold Axis

SAMPLE PREPARATION

Thin Sections

Samples were cut into three mutually perpendicular billets from a handspecimen block or 1.0 inch diameter drill core (Fig. A.2). The three sections orientations that were used are as follows:

b-section = Bedding-parallel, looking down into bedding.
p-section = Bedding- and dip-perpendicular, looking through the updip surface in the downdip direction.
v-section = Bedding-perpendicular and dip-parallel, looking northeast through the southwest face.

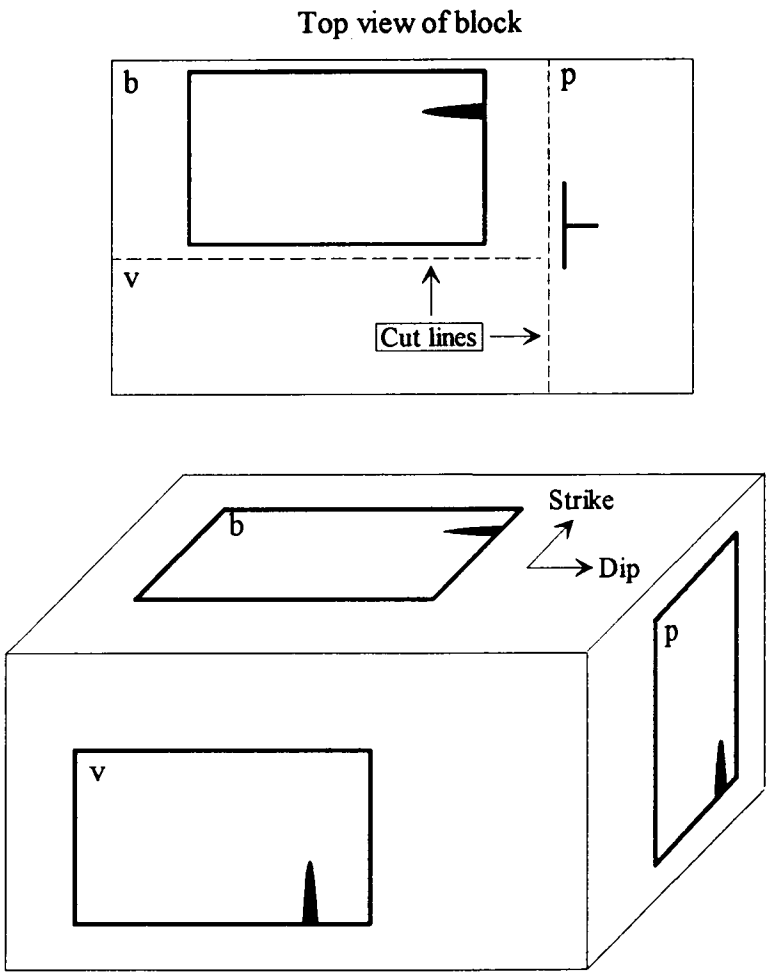

Fig. A.2. Block of Keefer Sandstone.

Notching convention

A small notch was cut into each billet so that later, while looking at the thin section, its relative orientation would be known. Billets were notched and mounted to glass slides as illustrated in Figure A.3.

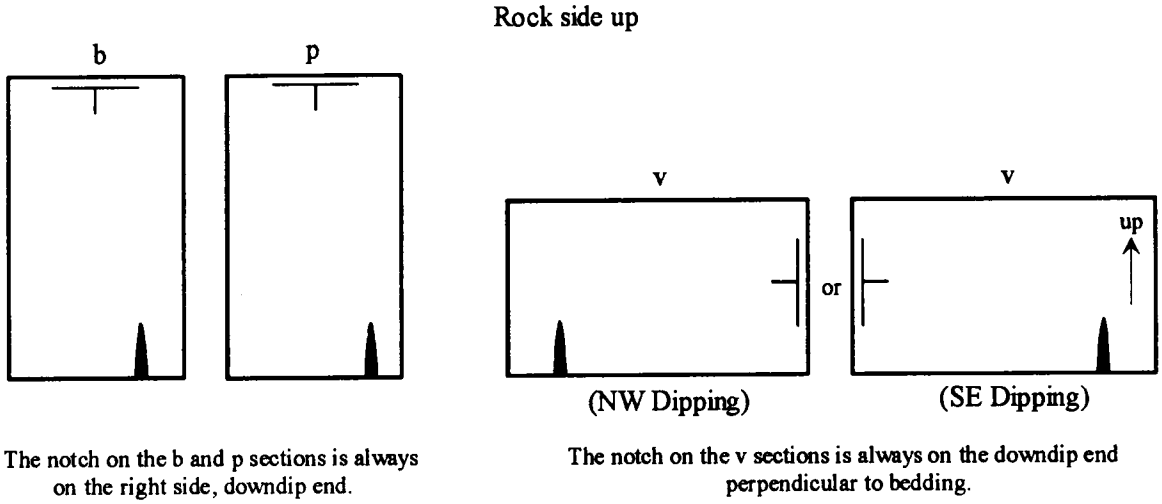

Fig. A.3. Orientation of billets on glass slides.

Thin section labels

An example of a thin section label is shown in Figure A.4.

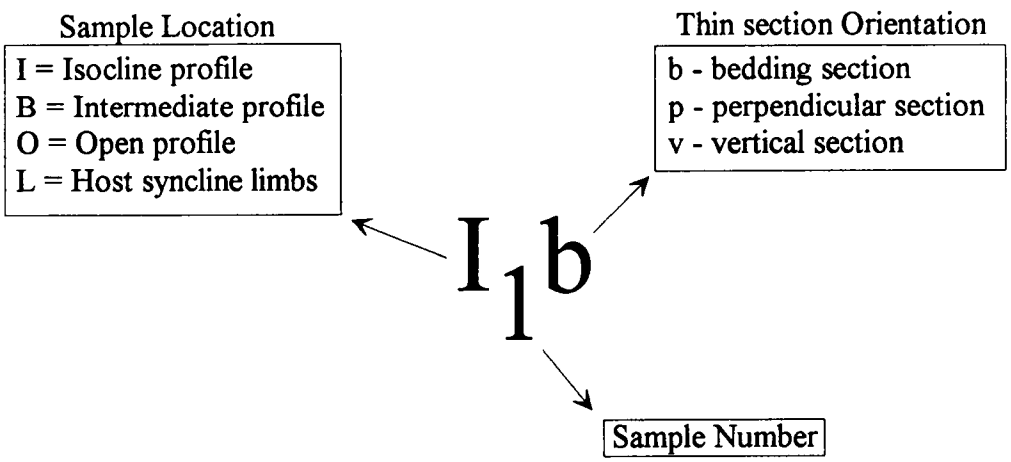

Fig. A.4. Sample labeling convention.

DATA COLLECTION

Cathodoluminescence Photomicroscopy

- 1-2 photographs taken, enough to ensure 150 grain minimum
- Ektachrome 400ASA film was used; exposed 1 stop down and pushed processed 1 stop.
- 2-3 minute exposure times.
- All thin sections were arranged in the cathodoluminoscope (Technosyn, MK2 and MK3) vacuum chamber with the notch towards the front (downdip end) (Fig. A.5).
- Orientation of the photographs correspond to the orientaion of the thin sections.

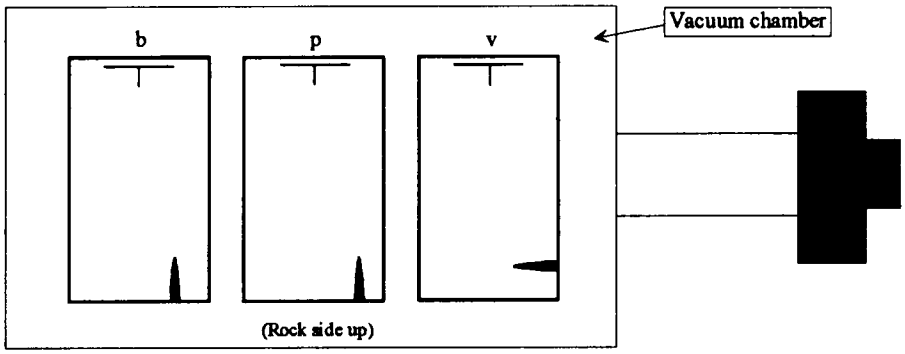

Fig. A.5. Set-up for CL photomicroscopy.

Polarized Light (PL) Photomicroscopy

- Photographed the exact same CL scenes.
- Arranged same as CL scenes.

Digitizing Grain Shapes

- Only the cathodoluminesence images were digitized.
- Xerox color prints (8.5"x11") were made for each slide photographed.
- The prints were arranged with the sample numbers at the top of the photo for strain analysis.
- Figure A.6 shows how the photographs were arranged on the digitizing pad and the relationship of the photographs to the dip direction of the sample.

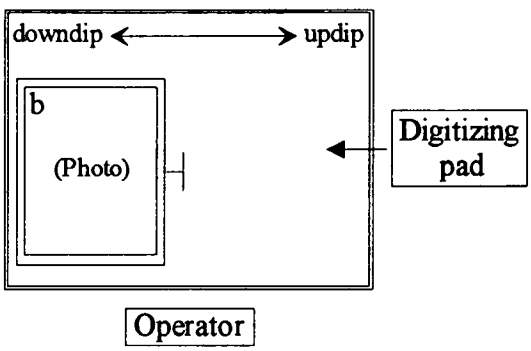

Fig. A.6. Orientation of photographs on the digitizing pad.

APPENDIX B: TWO- AND THREE-DIMENSIONAL ROTATED AND UNROTATED FINITE STRAIN DATA

This appendix contains processed finite strain data arranged by profile line. All data are from cathodoluminecent photomicrographs. Strain data with bedding rotated to horizontal are shown in the first half (Table B.2) and data with true field orientations are shown in the second half (Table B.3). A map depicting sample locations is included in Appendix A (Fig. A.1). Two-dimensional data is listed under the input data section. Each plane is represented by a letter: b (bed-parallel), p (bed-perpendicular, strike-parallel), and v (bed-perpendicular, dip-parallel). Three dimensional data is listed under Owens' output as: axial stretch, axis trend, axis plunge, and X/Y and Y/Z axial ratios. The last column, titled "Solution Used," refers to the solution generated by Owens' method which is the most statistically sound (contains the least error) (Owens 1984).

Table B.1 Sample labeling key

Sampling Label	Field Location	
L	Host syncline	
O	Open profile	(O-O')
M	Middle profile	(M-M')
I	Isocline profile	(I-I')
E	Extra anticline	(E-E')

Table B.2. Two- and three-dimensional rotated finite strain data.

Owens' Method Ellipsoid Calculations													
Input Data - Rotated to Horizontal							Owens' Output						
Sample Number	Orientation	Plane	Strike	Dip	Rake	R	Axis	Stretch	Axis Trend	Axis Plunge	Rxy	Ryz	Solution Used
L1rot	045/00	b	225	0	140.0	1.21	z	0.96	104.8	16.0	1.23	1.04	Q33
		p	45	90	29.0	1.13	y	1.00	222.1	57.9			
		v	135	90	127.5	1.12	x	1.23	6.4	27.0			
L2rot	055/00	b	235	0	88.0	1.10	z	0.80	311.8	71.8	1.05	1.25	Q33
		p	55	90	3.5	1.30	y	1.00	216.0	1.9			
		v	145	90	33.5	1.21	x	1.05	125.4	18.1			
L3rot	040/00	b	220	0	18.5	1.04	z	0.89	33.9	77.7	1.08	1.12	Q33
		p	40	90	170.0	1.24	y	1.00	133.0	2.0			
		v	130	90	1.5	1.09	x	1.08	223.4	12.1			
L4rot	045/00	b	45	0	7.5	1.11	z	0.93	71.8	67.7	1.12	1.08	Q33
		p	225	90	83.0	1.14	y	1.00	196.0	13.0			
		v	135	90	173.5	1.31	x	1.12	290.2	17.8			
L5rot	035/00	b	35	0	127.0	1.13	z	0.90	129.3	75.0	1.14	1.11	Q11
		p	215	90	175.5	1.22	y	1.00	262.5	10.4			
		v	125	90	159.0	1.15	x	1.14	354.5	10.7			
L6rot	041/00	b	41	0	175.0	1.07	z	0.82	77.1	68.3	1.07	1.21	Q33
		p	221	90	20.5	1.28	y	1.00	323.2	93.2			
		v	131	90	167.5	1.22	x	1.07	229.9	19.5			
O1rot	052/00	b	52	0	75.0	1.13	z	0.94	33.3	69.4	1.13	1.06	Q11
		p	232	90	19.0	1.06	y	1.00	218.9	20.5			
		v	142	90	3.5	1.18	x	1.13	128.2	1.9			
O2rot	065/00	b	65	0	142.0	1.25	z	0.92	126.1	11.0	1.21	1.09	Q12
		p	245	90	8.0	1.17	y	1.00	335.4	77.4			
		v	155	90	95.5	1.06	x	1.21	217.3	6.0			
O3rot	032/00	b	32	0	31.5	1.13	z	0.91	336.4	73.7	1.14	1.09	Q33
		p	212	90	5.5	1.24	y	1.00	143.3	15.9			
		v	122	90	15.0	1.09	x	1.14	234.3	3.5			
O4rot	039/00	b	39	0	143.0	1.04	z	0.84	95.2	47.4	1.24	1.20	Q33
		p	219	90	54.0	1.16	y	1.00	196.6	10.3			
		v	129	90	145.0	1.45	x	1.24	295.6	40.8			
O5rot	039/00	b	39	0	16.5	1.18	z	0.82	136.0	51.9	1.12	1.22	Q33
		p	219	90	179.0	1.13	y	1.00	7.8	25.8			
		v	129	90	148.0	1.31	x	1.12	264.2	25.9			
O6rot	035/00	b	35	0	120.5	1.14	z	0.84	174.2	83.0	1.19	1.20	Q33
		p	215	90	171.5	1.18	y	1.00	52.9	3.7			
		v	125	90	175.5	1.45	x	1.19	32.5	6.0			
O7rot	033/00	b	33	0	26.5	1.14	z	0.89	133.0	46.9	1.11	1.12	Q33
		p	213	90	2.5	1.18	y	1.00	338.8	40.1			
		v	123	90	130.0	1.14	x	1.11	237.5	13.2			

Owens' Method Ellipsoid Calculations

Sample		**Input Data - Rotated to Horizontal**					**Owens' Output**						
Number	Orientation	Plane	Strike	Dip	Rake	R	Axis	Stretch	Axis Trend	Axis Plunge	Rxy	Ryz	Solution Used
O8rot	034/00	b	214	0	8.5	1.20	z	0.93	319.6	33.3	1.12	1.08	Q11
		p	34	90	73.0	1.03	y	1.00	187.3	45.7			
		v	124	90	22.5	1.12	x	1.12	67.9	25.6			
O9rot	032/00	b	212	0	70.0	1.16	z	0.99	334.1	79.7	1.15	1.01	Q33
		p	32	90	4.5	1.04	y	1.00	190.2	8.4			
		v	122	90	8.0	1.13	x	1.15	99.3	6.0			
O10rot	031/00	b	211	0	147.0	1.14	z	0.94	244.3	59.5	1.14	1.07	Q33
		p	31	90	20.5	1.18	y	1.00	100.7	25.4			
		v	121	90	2.5	1.06	x	1.14	3.0	15.8			
M1rot	337/00	b	157	0	1.0	1.03	z	0.90	224.3	60.3	1.03	1.11	Q33
		p	337	90	17.0	1.10	y	1.00	110.7	12.9			
		v	67	90	27.5	1.12	x	1.03	14.2	26.3			
M2rot	020/00	b	200	0	175.0	1.10	z	0.94	301.2	31.2	1.13	1.06	Q33
		p	20	90	157.5	1.16	y	1.00	64.5	42.2			
		v	110	90	72.0	1.11	x	1.13	188.9	32.0			
M3rot	021/00	b	201	0	42.0	1.05	z	0.98	319.8	81.5	1.07	1.02	Q33
		p	21	90	0.0	1.06	y	1.00	152.7	8.3			
		v	111	90	5.0	1.05	x	1.07	62.4	1.9			
M4rot	030/00	b	210	0	125.5	1.09	z	0.95	66.6	28.4	1.05	1.06	Q33
		p	30	90	119.5	1.03	y	1.00	215.8	57.9			
		v	120	90	154.0	1.06	x	1.05	328.9	13.8			
M5rot	012/00	b	192	0	117.5	1.22	z	0.83	251.2	72.2	1.19	1.21	Q33
		p	12	90	4.5	1.28	y	1.00	44.8	16.0			
		v	102	90	16.5	1.31	x	1.19	136.9	7.5			
M6rot	041/00	b	41	0	165.0	1.20	z	0.84	296.3	86.2	1.15	1.18	Q33
		p	221	90	179.5	1.22	y	1.00	98.9	3.6			
		v	131	90	2.5	1.28	x	1.15	188.9	1.1			
M7rot	024/00	b	24	0	6.5	1.19	z	0.95	305.4	19.3	1.11	1.05	Q33
		p	204	90	26.5	1.08	y	1.00	92.8	67.5			
		v	114	90	46.5	1.03	x	1.11	211.4	11.3			
M8rot	011/00	b	11	0	150.5	1.26	z	0.92	90.0	53.2	1.27	1.08	Q33
		p	191	90	158.0	1.15	y	1.00	228.9	29.4			
		v	101	90	152.5	1.21	x	1.27	330.8	20.0			
M9rot	012/00	b	12	0	16.5	1.15	z	0.92	207.0	81.9	1.12	1.09	Q33
		p	192	90	151.0	1.09	y	1.00	317.9	2.9			
		v	102	90	3.0	1.18	x	1.12	48.3	7.6			
M10rot	021/00	b	21	0	4.5	1.06	z	0.87	331.0	55.7	1.05	1.15	Q33
		p	201	90	44.0	1.13	y	1.00	68.1	4.8			
		v	111	90	22.0	1.18	x	1.05	161.3	33.8			

Table B.2. continued...

Owens' Method Ellipsoid Calculations													
Input Data - Rotated to Horizontal							Owens' Output						
Sample Number	Orientation	Plane	Strike	Dip	Rake	R	Axis	Stretch	Axis Trend	Axis Plunge	Rxy	Ryz	Solution Used
I1rot	037/00	b	37	0	20.5	1.25	z	0.96	297.1	61.7	1.26	1.05	Q33
		p	217	90	155.0	1.19	y	1.00	162.7	20.6			
		v	127	90	23.0	1.12	x	1.26	65.5	18.5			
I2rot	019/00	b	19	0	6.0	1.09	z	0.83	87.9	74.8	1.07	1.21	Q33
		p	199	90	7.0	1.26	y	1.00	305.4	12.2			
		v	109	90	166.5	1.22	x	1.07	213.5	9.0			
I3rot	034/00	b	34	0	154.0	1.13	z	0.88	245.8	52.3	1.16	1.13	Q33
		p	214	90	148.0	1.29	y	1.00	123.6	22.4			
		v	124	90	20.0	1.07	x	1.16	20.6	28.5			
I4rot	029/00	b	29	0	150.0	1.14	z	0.91	27.0	76.5	1.21	1.09	Q12
		p	209	90	14.0	1.17	y	1.00	249.6	10.0			
		v	119	90	6.0	1.21	x	1.21	158.0	9.0			
I5rot	028/00	b	28	0	168.5	1.15	z	0.91	106.0	55.3	1.09	1.10	Q11
		p	208	90	3.5	1.14	y	1.00	280.8	34.6			
		v	118	90	153.5	1.11	x	1.09	12.5	2.4			
I6rot	049/00	b	49	0	124.0	1.06	z	0.86	87.8	57.0	1.05	1.16	Q12
		p	229	90	29.0	1.14	y	1.00	217.4	22.5			
		v	139	90	158.5	1.19	x	1.05	317.4	22.8			
I7rot	043/00	b	43	0	140.0	1.09	z	0.93	16.8	72.0	1.12	1.08	Q33
		p	223	90	17.0	1.17	y	1.00	208.1	2.2			
		v	133	90	17.5	1.10	x	1.12	189.4	17.9			
I8rot	012/00	b	12	0	178.0	1.13	z	0.84	95.4	59.1	1.12	1.19	Q33
		p	192	90	3.5	1.32	y	1.00	286.9	30.4			
		v	102	90	140.5	1.17	x	1.12	193.9	5.0			
I9rot	028/00	b	28	0	163.0	1.11	z	0.86	107.2	56.4	1.06	1.16	Q33
		p	208	90	2.0	1.13	y	1.00	253.5	29.0			
		v	118	90	151.0	1.19	x	1.06	352.4	15.6			
I10rot	031/00	b	31	0	5.0	1.18	z	0.80	138.0	39.8	1.13	1.24	Q23
		p	211	90	135.0	1.20	y	1.00	243.8	18.1			
		v	121	90	135.0	1.28	x	1.13	352.6	44.7			
I11rot	034/00	b	34	0	155.0	1.13	z	0.87	240.0	61.2	1.11	1.14	Q33
		p	214	90	136.0	1.14	y	1.00	84.8	26.5			
		v	124	90	4.0	1.21	x	1.11	349.6	10.4			
I12rot	040/00	b	40	0	58.0	1.04	z	0.76	319.1	60.0	1.05	1.31	Q33
		p	220	90	3.0	1.28	y	1.00	203.6	13.9			
		v	130	90	35.0	1.34	x	1.05	106.6	26.0			
I13rot	041/00	b	221	0	12.5	1.17	z	0.89	12.8	86.3	1.11	1.12	Q33
		p	41	90	145.0	1.05	y	1.00	166.9	3.4			
		v	131	90	0.5	1.23	x	1.11	256.9	1.6			

Owens' Method Ellipsoid Calculations

		Input Data - Rotated to Horizontal					**Owens' Output**						
Sample Number	Orientation	Plane	Strike	Dip	Rake	R	Axis	Stretch	Axis Trend	Axis Plunge	Rxy	Ryz	Solution Used
I14rot	036/00	b	216	0	151.0	1.22	z	0.88	81.8	85.7	1.19	1.14	Q11
		p	36	90	177.0	1.19	y	1.00	261.4	4.3			
		v	126	90	178.5	1.29	x	1.19	351.4	0.0			
I15rot	049/00	b	229	0	96.0	1.18	z	0.87	35.3	47.8	1.16	1.16	Q33
		p	49	90	142.0	1.21	y	1.00	271.3	26.9			
		v	139	90	31.0	1.19	x	1.16	164.5	29.8			
I16rot	043/00	b		0			z						
		p		90			y						
		v		90			x						
I17rot	013/00	b	13	0	157.0	1.07	z	0.87	46.2	62.4	1.07	1.16	Q33
		p	193	90	24.0	1.22	y	1.00	280.5	17.0			
		v	103	90	165.5	1.13	x	1.07	183.8	21.1			
I18rot	050/00	b		0			z						
		p		90			y						
		v		90			x						
I19rot	040/00	b	40	0	150.0	1.10	z	0.96	274.8	73.7	1.11	1.05	Q33
		p	220	90	175.0	1.16	y	1.00	109.8	15.8			
		v	130	90	17.0	1.04	x	1.11	18.7	4.0			
I20rot	050/00	b	50	0	145.0	1.05	z	0.85	136.8	63.7	1.07	1.18	Q33
		p	230	90	177.5	1.14	y	1.00	250.9	11.4			
		v	140	90	155.0	1.25	x	1.07	345.9	23.3			
I21rot	035/00	b	35	0	20.0	1.18	z	0.87	155.7	30.7	1.04	1.15	Q33
		p	215	90	116.5	1.07	y	1.00	323.4	58.7			
		v	125	90	142.0	1.11	x	1.04	62.5	5.7			
I22rot	120/00	b		0			z						
		p		90			y						
		v		90			x						
I23rot	035/00	b		0			z						
		p		90			y						
		v		90			x						
I24rot	045/00	b		0			z						
		p		90			y						
		v		90			x						
E1rot	021/00	b	21	0	27.5	1.25	z	0.93	323.6	22.8	1.25	1.07	Q33
		p	201	90	106.0	1.10	y	1.00	201.7	51.5			
		v	111	90	30.0	1.18	x	1.25	67.2	29.2			
E2rot	032/00	b	212	0	131.5	1.09	z	0.90	325.3	66.7	1.15	1.11	Q33
		p	32	90	157.5	1.12	y	1.00	61.5	2.6			
		v	122	90	21.5	1.24	x	1.15	152.6	23.1			

Table B.2. continued...

Owens' Method Ellipsoid Calculations

Input Data - Rotated to Horizontal							Owens' Output						
Sample Number	Orientation	Plane	Strike	Dip	Rake	R	Axis	Stretch	Axis Trend	Axis Plunge	Rxy	Ryz	Solution Used
E3rot	042/00	b	222	0	18.0	1.16	z	0.95	114.5	58.0	1.18	1.06	Q33
		p	42	90	157.5	1.19	y	1.00	345.1	21.6			
		v	132	90	146.5	1.10	x	1.18	245.7	22.4			
E4rot	038/00	b	38	0	4.5	1.16	z	0.88	359.9	62.2	1.13	1.13	Q33
		p	218	90	36.0	1.21	y	1.00	121.3	15.3			
		v	128	90	12.0	1.14	x	1.13	217.8	22.6			

Table B.3. Two- and three-dimensional unrotated finite strain data.

Owens' Method Ellipsoid Calculations

Sample	Input Data						Owens' Output						
Number	Orientation	Plane	Strike	Dip	Rake	R	Axis	Stretch	Axis Trend	Axis Plunge	Rxy	Ryz	Solution Used
L1	045/87	b	225	87	140.0	1.21	z	0.96	257.8	54.8	1.23	1.04	Q33
		p	45	3	29.0	1.13	y	1.00	166.9	0.6			
		v	135	90	40.5	1.12	x	1.23	76.5	35.2			
L2	055/89	b	235	89	92.0	1.10	z	0.81	150.7	21.6	1.02	1.24	Q33
		p	55	1	3.5	1.30	y	1.00	58.1	6.5			
		v	145	90	123.5	1.21	x	1.02	312.2	67.3			
L3	040/68	b	220	68	18.5	1.04	z	0.89	116.6	23.4	1.08	1.12	Q33
		p	40	22	170.0	1.24	y	1.00	315.8	65.4			
		v	130	90	113.5	1.09	x	1.08	209.7	7.2			
L4	045/50	b	45	50	7.5	1.11	z	0.89	145.3	45.4	1.16	1.12	Q33
		p	225	40	83.0	1.14	y	1.00	45.7	9.3			
		v	135	90	43.5	1.31	x	1.16	306.9	43.1			
L5	035/50	b	35	50	127.0	1.13	z	0.90	304.1	55.9	1.15	1.11	Q33
		p	215	40	175.5	1.22	y	1.00	78.3	25.3			
		v	125	90	29.0	1.15	x	1.15	179.0	21.3			
L6	041/62	b	41	62	175.0	1.07	z	0.82	333.7	39.2	1.07	1.22	Q33
		p	221	28	20.5	1.28	y	1.00	150.8	50.8			
		v	131	90	49.5	1.22	x	1.07	242.5	1.4			
O1	052/24	b	52	24	75.0	1.13	z	0.95	17.6	77.4	1.15	1.05	Q33
		p	232	66	19.0	1.06	y	1.00	216.2	12.0			
		v	142	90	3.5	1.18	x	1.15	125.4	3.9			
O2	065/22	b	65	22	142.0	1.25	z	0.92	119.5	34.4	1.19	1.08	Q33
		p	245	68	8.0	1.17	y	1.00	330.8	51.3			
		v	155	90	117.5	1.06	x	1.19	220.5	15.5			
O3	032/18	b	32	18	31.5	1.13	z	0.91	319.1	57.6	1.14	1.09	Q33
		p	212	72	5.5	1.24	y	1.00	146.4	32.2			
		v	122	90	33.0	1.09	x	1.14	54.3	3.3			
O4	039/17	b	39	17	143.0	1.04	z	0.84	80.3	60.2	1.24	1.20	Q33
		p	219	73	54.0	1.16	y	1.00	200.5	16.0			
		v	129	90	162.0	1.45	x	1.24	297.9	24.4			
O5	039/20	b	39	20	16.5	1.18	z	0.08	150.0	70.6	1.10	1.24	Q33
		p	219	70	179.0	1.13	y	1.00	2.6	16.5			
		v	129	90	168.0	1.31	x	1.10	269.7	9.9			
O6	035/10	b	35	10	120.5	1.14	z	0.83	152.8	83.5	1.21	1.20	Q33
		p	215	80	171.5	1.18	y	1.00	54.2	1.0			
		v	125	90	175.5	1.45	x	1.21	324.1	6.4			
O7	033/02	b	33	2	26.5	1.14	z	0.89	133.4	48.9	1.11	1.12	Q33
		p	213	88	2.5	1.18	y	1.00	337.9	38.5			
		v	123	90	132.0	1.14	x	1.11	237.9	12.4			

Owens' Method Ellipsoid Calculations

Input Data							Owens' Output						
Sample Number	Orientation	Plane	Strike	Dip	Rake	R	Axis	Stretch	Axis Trend	Axis Plunge	Rxy	Ryz	Solution Used
O8	034/08	b	214	8	8.5	1.20	z	0.92	307.9	51.8	1.11	1.08	Q33
		p	34	82	73.0	1.03	y	1.00	167.4	31.3			
		v	124	90	14.5	1.12	x	1.11	64.9	19.7			
O9	032/34	b	212	34	70.0	1.16	z	0.99	108.4	64.4	1.15	1.01	Q33
		p	32	56	4.5	1.04	y	1.00	9.0	4.5			
		v	122	90	154.0	1.13	x	1.15	276.9	25.1			
O10	031/40	b	211	40	147.0	1.14	z	0.94	172.3	57.1	1.14	1.07	Q33
		p	31	50	20.5	1.18	y	1.00	282.3	12.5			
		v	121	90	142.5	1.06	x	1.14	19.6	29.9			
M1	337/17	b	157	17	1.0	1.03	z	0.90	200.8	74.6	1.03	1.11	Q33
		p	337	73	17.0	1.10	y	1.00	109.4	0.4			
		v	67	90	10.5	1.12	x	1.03	19.3	15.4			
M2	020/42	b	200	42	175.0	1.10	z	0.94	320.6	71.2	1.13	1.06	Q33
		p	20	48	157.5	1.16	y	1.00	77.3	8.7			
		v	110	90	30.0	1.11	x	1.13	169.9	16.5			
M3	021/43	b	201	43	42.0	1.07	z	0.98	104.0	54.3	1.07	1.02	Q33
		p	21	47	0.0	1.06	y	1.00	336.8	23.5			
		v	111	90	142.0	1.05	x	1.07	235.0	25.3			
M4	030/67	b	210	67	125.5	1.09	z	0.97	216.6	40.1	1.08	1.03	Q33
		p	30	23	119.5	1.03	y	1.00	88.1	36.5			
		v	120	90	154.0	1.06	x	1.08	334.1	28.8			
M5	012/41	b	192	41	117.5	1.22	z	0.82	122.9	63.5	1.19	1.21	Q33
		p	12	49	4.5	1.28	y	1.00	227.6	7.2			
		v	102	90	155.5	1.31	x	1.19	321.0	25.4			
M6	041/38	b	41	38	1.0	1.20	z	0.83	310.6	51.6	1.09	1.21	Q33
		p	221	52	179.5	1.22	y	1.00	134.9	38.3			
		v	131	90	40.5	1.28	x	1.09	43.3	2.1			
M7	024/20	b	24	20	6.5	1.19	z	0.95	124.7	1.4	1.11	1.05	Q33
		p	204	70	26.5	1.08	y	1.00	25.2	81.7			
		v	114	90	66.5	1.03	x	1.11	214.9	8.2			
M8	011/03	b	11	3	150.5	1.26	z	0.92	89.1	56.1	1.27	1.08	Q33
		p	191	87	158.0	1.15	y	1.00	230.2	27.6			
		v	101	90	155.5	1.21	x	1.27	330.0	18.1			
M9	012/01	b	12	1	16.5	1.15	z	0.92	212.2	81.6	1.12	1.09	Q33
		p	192	89	151.0	1.09	y	1.00	317.8	2.3			
		v	102	90	4.0	1.18	x	1.12	48.2	8.1			
M10	021/34	b	21	34	4.5	1.06	z	0.87	315.6	26.9	1.05	1.14	Q33
		p	201	56	44.0	1.13	y	1.00	62.9	30.3			
		v	111	90	56.0	1.18	x	1.05	192.2	47.3			

Table B.3. continued

Owens' Method Ellipsoid Calculations

Sample Number	Orientation	Input Data Plane	Strike	Dip	Rake	R	Owens' Output Axis	Stretch	Axis Trend	Axis Plunge	Rxy	Ryz	Solution Used
I1	037/25	b	37	25	20.5	1.25	z	0.96	300.5	37.8	1.26	1.04	Q33
		p	217	65	155.0	1.19	y	1.00	171.3	39.1			
		v	127	90	48.0	1.12	x	1.26	55.2	28.4			
I2	019/65	b	19	65	6.0	1.09	z	0.83	296.0	39.2	1.07	1.21	Q33
		p	199	25	7.0	1.26	y	1.00	134.2	49.4			
		v	109	90	51.5	1.22	x	1.07	33.5	9.0			
I3	034/86	b	34	86	26.0	1.13	z	0.92	272.2	5.3	1.21	1.09	Q33
		p	214	4	148.0	1.29	y	1.00	168.7	68.2			
		v	124	90	106.0	1.07	x	1.21	4.3	21.1			
I4	029/61	b	29	61	150.0	1.14	z	0.89	309.0	24.8	1.14	1.12	Q33
		p	209	29	14.0	1.17	y	1.00	60.8	38.7			
		v	119	90	67.0	1.21	x	1.14	195.2	41.1			
I5	028/72	b	28	72	168.5	1.15	z	0.91	309.4	52.2	1.09	1.10	Q33
		p	208	18	3.5	1.14	y	1.00	100.8	34.2			
		v	118	90	45.0	1.11	x	1.09	200.6	14.1			
I6	049/03	b	49	3	124.0	1.06	z	0.86	86.5	59.1	1.04	1.17	Q33
		p	229	87	29.0	1.14	y	1.00	220.1	22.4			
		v	139	90	161.5	1.19	x	1.04	318.8	20.1			
I7	043/86	b	43	86	140.0	1.09	z	0.93	149.1	4.1	1.12	1.08	Q33
		p	223	4	17.0	1.17	y	1.00	53.0	56.6			
		v	133	90	103.5	1.10	x	1.12	241.8	33.1			
I8	012/64	b	12	64	178.0	1.13	z	0.84	288.3	57.7	1.12	1.19	Q33
		p	192	26	3.5	1.32	y	1.00	107.2	32.3			
		v	102	90	24.5	1.17	x	1.12	197.5	0.5			
I9	028/52	b	28	52	163.0	1.11	z	0.87	102.3	70.1	1.04	1.15	Q33
		p	208	38	2.0	1.13	y	1.00	298.6	19.2			
		v	118	90	23.0	1.19	x	1.04	206.8	5.2			
I10	031/69	b	31	69	5.0	1.18	z	0.82	262.8	65.0	1.15	1.22	Q33
		p	211	21	135.0	1.20	y	1.00	67.7	24.3			
		v	121	90	24.0	1.28	x	1.15	160.3	5.8			
I11	034/58	b	34	58	155.0	1.13	z	0.89	275.9	18.8	1.12	1.12	Q33
		p	214	32	136.0	1.14	y	1.00	38.5	57.6			
		v	124	90	62.0	1.21	x	1.12	176.6	25.3			
I12	040/81	b	40	81	58.0	1.04	z	0.76	135.0	21.5	1.04	1.31	Q33
		p	220	9	3.0	1.28	y	1.00	233.5	20.4			
		v	130	90	116.0	1.34	x	1.04	2.8	59.6			
I13	041/67	b	221	67	12.5	1.17	z	0.90	123.4	34.2	1.11	1.11	Q33
		p	41	23	145.0	1.05	y	1.00	355.6	42.0			
		v	131	90	113.5	1.23	x	1.11	235.6	29.0			

Owens' Method Ellipsoid Calculations

Sample		Input Data					Owens' Output						
Number	Orientation	Plane	Strike	Dip	Rake	R	Axis	Stretch	Axis Trend	Axis Plunge	Rxy	Ryz	Solution Used
I14	036/67	b	216	67	151.0	1.22	z	0.88	123.5	21.6	1.21	1.13	Q33
		p	36	23	177.0	1.19	y	1.00	235.3	43.2			
		v	126	90	111.5	1.29	x	1.21	14.8	39.0			
I15	049/67	b	229	67	96.0	1.18	z	0.87	92.0	26.1	1.16	1.15	Q33
		p	49	23	142.0	1.21	y	1.00	214.5	47.6			
		v	139	90	144.0	1.19	x	1.16	345.1	30.7			
I16	043/43	b		0			z						
		p		90			y						
		v		90			x						
I17	013/72	b	13	72	157.0	1.07	z	0.89	259.3	25.2	1.11	1.12	Q33
		p	193	18	156.0	1.22	y	1.00	44.6	60.2			
		v	103	90	57.5	1.13	x	1.11	162.1	14.8			
I18	050/28	b		0			z						
		p		90			y						
		v		90			x						
I19	040/10	b	40	10	150.0	1.10	z	0.96	287.5	65.2	1.11	1.05	Q33
		p	220	80	175.0	1.16	y	1.00	108.5	24.9			
		v	130	90	27.0	1.04	x	1.11	18.3	0.4			
I20	050/15	b	50	15	145.0	1.05	z	0.85	132.8	78.7	1.07	1.18	Q33
		p	230	75	177.5	1.14	y	1.00	253.0	5.7			
		v	140	90	170.0	1.25	x	1.07	344.0	9.7			
I21	035/20	b	35	20	20.0	1.18	z	0.96	133.4	58.4	1.19	1.04	Q33
		p	215	70	38.0	1.13	y	1.00	350.5	26.1			
		v	125	90	162.0	1.11	x	1.19	252.1	16.5			
I22	120/4	b		0			z						
		p		90			y						
		v		90			x						
I23	035/20	b		0			z						
		p		90			y						
		v		90			x						
I24	045/15	b		0			z						
		p		90			y						
		v		90			x						
E1	021/37	b	21	37	27.5	1.25	z	0.93	145.0	13.3	1.23	1.07	Q33
		p	201	53	106.0	1.10	y	1.00	245.7	38.1			
		v	111	90	67.0	1.18	x	1.23	39.4	48.8			
E2	032/35	b	212	35	131.5	1.09	z	0.90	81.6	78.5	1.16	1.11	Q33
		p	32	55	157.5	1.12	y	1.00	239.5	10.7			
		v	122	90	171.5	1.24	x	1.16	330.3	4.2			

Table B.3. continued...

Owens' Method Ellipsoid Calculations

Input Data							Owens' Output						
Sample Number	Orientation	Plane	Strike	Dip	Rake	R	Axis	Stretch	Axis Trend	Axis Plunge	Rxy	Ryz	Solution Used
E3	042/45	b	222	45	18.0	1.16	z	0.95	122.5	14.0	1.18	1.06	Q33
		p	42	45	157.5	1.19	y	1.00	12.2	54.3			
		v	132	90	101.5	1.10	x	1.18	221.5	32.1			
E4	038/28	b	38	28	4.5	1.16	z	0.89	338.2	42.1	1.13	1.13	Q33
		p	218	62	36.0	1.21	y	1.00	122.0	41.8			
		v	128	90	40.0	1.14	x	1.13	230.0	19.1			

APPENDIX C: TWO- AND THREE-DIMENSIONAL ROTATED PSS INCREMENTAL STRAIN DATA

This appendix contains incremental strain data from grain to grain solution (Onasch in press) arranged by profile lines. All data are derived from application of the PSS method (Onasch in press). Cathodoluminecent photomicrographs were used to define original grain shapes. These incremental strains were processed with bedding restored to the horizontal. Again, Figure A.1 in Appendix A shows sample locations. As with the finite strain data, the two-dimensional data is listed under the input data section. Each plane is represented by a letter: b (bed-parallel), p (bed-perpendicular, strike-parallel), and v (bed-perpendicular, dip-parallel). Three dimensional data is listed under Owens' output as: axial stretch, axis trend, axis plunge, and X/Y and Y/Z axial ratios. The last column, titled "Solution Used," refers to the solution generated by Owens' method which is the most statistically sound (contains the least error) (Owens 1984).

Table C.1. Two- and three-dimensional rotated PSS incremental strain data.

Owens' Method PSS Strain Ellipsoid Calculations													
	Input Data Rotated to Horizontal						Owens' Output						
Sample Number	Orientation	Plane	Strike	Dip	Rake	R	Axis	Stretch	Axis Trend	Axis Plunge	Rxy	Ryz	Solution Used
						Host Syncline							
L1rot	045/00	b	225	0	0.0	1.11	z	0.99	316.7	90.0	1.09	1.01	Q33
		p	45	90	0.0	1.08	y	1.00	135.0	0.0			
		v	135	90	0.0	1.02	x	1.09	225.0	0.0			
L2rot	055/00	b	235	0	0.0	1.07	z	0.98	145.0	90.0	1.07	1.02	Q33
		p	55	90	0.0	1.10	y	1.00	325.0	0.0			
		v	145	90	0.0	1.02	x	1.07	225.0	0.0			
L3rot	040/00	b	220	0	0.0	1.12	z	0.96	130.0	0.0	1.06	1.04	Q33
		p	40	90	0.0	1.05	y	1.00	273.4	90.0			
		v	130	90	90.0	1.03	x	1.06	40.0	0.0			
						O-O' Profile							
O2rot	065/00	b	65	0	0.0	1.04	z	0.99	176.9	90.0	1.04	1.01	Q12
		p	245	90	0.0	1.06	y	1.00	335.0	0.0			
		v	155	90	0.0	1.01	x	1.04	65.0	0.0			
O3rot	032/00	b	32	0	90.0	1.02	z	0.89	298.1	90.0	1.00	1.12	Q33
		p	212	90	0.0	1.14	y	1.00	32.0	0.0			
		v	122	90	0.0	1.11	x	1.00	122.0	0.0			
O5rot	039/00	b	39	0	0.0	1.04	z	0.98	356.9	90.0	1.01	1.02	Q33
		p	219	90	0.0	1.00	y	1.00	129.0	0.0			
		v	129	90	0.0	1.05	x	1.01	219.0	0.0			
O6rot	035/00	b	35	0	0.0	1.01	z	0.96	52.1	90.0	1.01	1.04	Q33
		p	215	90	0.0	1.02	y	1.00	215.0	0.0			
		v	125	90	0.0	1.06	x	1.01	305.0	0.0			
O9rot	032/00	b	212	0	0.0	1.02	z	0.96	116.0	90.0	1.00	1.04	Q33
		p	32	90	0.0	1.02	y	1.00	212.0	0.0			
		v	122	90	0.0	1.06	x	1.00	302.0	0.0			
						M-M' Profile							
M1rot	337/00	b	157	0	0.0	1.07	z	0.96	50.5	90.0	1.04	1.05	Q33
		p	337	90	0.0	1.06	y	1.00	247.0	0.0			
		v	67	90	0.0	1.07	x	1.04	157.0	0.0			
M2rot	020/00	b	200	0	0.0	1.07	z	0.96	270.1	90.0	1.07	1.02	Q33
		p	20	90	0.0	1.10	y	1.00	110.0	0.0			
		v	110	90	0.0	1.04	x	1.07	20.0	0.0			
M3rot	021/00	b	201	0	0.0	1.03	z	0.93	134.2	90.0	1.04	1.08	Q33
		p	21	90	0.0	1.12	y	1.00	291.0	0.0			
		v	111	90	0.0	1.07	x	1.04	21.0	0.0			
						I-I' Profile							
I4rot	029/00	b	29	0	0.0	1.02	z	0.99	129.2	90.0	1.03	1.01	Q12
		p	209	90	0.0	1.04	y	1.00	299.0	0.0			
		v	119	90	0.0	1.00	x	1.03	29.0	0.0			

Owens' Method PSS Strain Ellipsoid Calculations													
Input Data Rotated to Horizontal							Owens' Output						
Sample Number	Orientation	Plane	Strike	Dip	Rake	R	Axis	Stretch	Axis Trend	Axis Plunge	Rxy	Ryz	Solution Used
I-I' Profile continued													
I6rot	049/00	b	49	0	0.0	1.05	z	0.94	139.0	55.1	1.02	1.06	Q12
		p	229	90	0.0	1.06	y	1.00	319.0	34.9			
		v	139	90	149.0	1.06	x	1.02	49.0	0.0			
I9rot	028/00	b	28	0	0.0	1.06	z	0.94	256.2	90.0	1.04	1.07	Q33
		p	208	90	0.0	1.10	y	1.00	118.0	0.0			
		v	118	90	0.0	1.08	x	1.04	28.0	0.0			
I10rot	031/00	b	31	0	139.0	1.06	z	0.96	96.1	46.2	1.05	1.04	Q23
		p	211	90	0.0	1.04	y	1.00	242.6	38.6			
		v	121	90	142.0	1.06	x	1.05	347.1	17.4			
I11rot	034/00	b	34	0	155.0	1.08	z	0.96	105.1	57.4	1.07	1.04	Q33
		p	214	90	0.0	1.07	y	1.00	268.9	31.6			
		v	124	90	157.0	1.06	x	1.07	3.5	7.4			
I12rot	040/00	b	40	0	148.0	1.07	z	0.97	287.9	90.0	1.07	1.03	Q33
		p	220	90	0.0	1.06	y	1.00	89.4	0.0			
		v	130	90	0.0	1.07	x	1.07	179.4	0.0			
I13rot	041/00	b	221	0	0.0	1.06	z	0.96	41.0	82.6	1.03	1.05	Q33
		p	41	90	152.0	1.04	y	1.00	131.0	0.0			
		v	131	90	0.0	1.07	x	1.03	221.0	7.4			
I14rot	036/00	b	216	0	0.0	1.07	z	0.99	325.0	90.0	1.07	1.01	Q11
		p	36	90	0.0	1.07	y	1.00	139.0	0.0			
		v	126	90	0.0	1.01	x	1.07	229.0	0.0			
I19rot	040/00	b	40	0	0.0	1.04	z	0.96	28.0	90.0	1.01	1.04	Q33
		p	220	90	0.0	1.02	y	1.00	130.0	0.0			
		v	130	90	0.0	1.07	x	1.01	220.0	0.0			
I20rot	050/00	b	50	0	0.0	1.01	z	0.99	304.5	90.0	1.00	1.01	Q33
		p	230	90	0.0	1.01	y	1.00	140.0	0.0			
		v	140	90	0.0	1.02	x	1.00	50.0	0.0			

VITA

Anthony John Caldanaro Jr. was born on Friday, September 20, 1968 at St. Margaret's Hospital in Hammond, Indiana. When he was less than three months old, Anthony was moved from St. Johns, Indiana to LeRoy, Illinois. At a young age Anthony was diagnosed with asthma. Anthony attended LeRoy Elementary until the fourth grade when, in 1977, Anthony and his family moved to Findlay, Ohio where his father had accepted a job with Marathon Oil. Anthony continued his pre-high school education at Liberty-Benton Elementary. In 1986, Anthony graduated from Liberty-Benton High School and started college at Bowling Green State University, Bowling Green, Ohio. In the fall of 1988, he took undergraduate structural geology and met Dr. Charles M. Onasch, who forever warped him. After attending field camp in 1989, Anthony's enthusiasm for geology and especially field work intensified. During his last semester as an undergraduate Anthony was awarded a NAGT summer internship with the USGS in Denver, Colorado. Most of this summer experience was spent in the beautiful state of Idaho, where he sampled stream sediments in remote locations, sometimes accessible only by helicopter. Two days after leaving Denver, Anthony arrived in Knoxville to attend graduate school at the University of Tennessee. In the spring of 1994 Anthony J. Caldanaro Jr. received his Master of Science degree from the Department of Geological Sciences, University of Tennessee, Knoxville.